Master thesis and internship[BR]- Master's thesis : Stagnation line aerothermochemistry. Focus on uncertainty quantification in nitrogen plasma-graphite interactions in VKI Plasmatron[BR]- Internship

Auteur : Bandera, Matteo
Promoteur(s) : Arnst, Maarten
Faculté : Faculté des Sciences appliquées
Diplôme : Master en ingénieur civil en aérospatiale, à finalité spécialisée en "aerospace engineering"
Année académique : 2023-2024
URI/URL : http://hdl.handle.net/2268.2/20860

LIÈGE université

von KARMAN INSTITUTE FOR FLUID DYNAMICS

Stagnation line aerothermochemistry. Focus on uncertainty quantification in nitrogen plasma-graphite interactions in VKI Plasmatron

Master's thesis completed in order to obtain the degree of Master of Science in Aerospace Engineering
University of Liège - Faculty of Applied Sciences

by: **Matteo Bandera**

Student ID: s224977
Advisor: Prof. Arnst Maarten
Co-advisors: Prof. Vigevano Luigi, Prof. Magin Thierry, Bariselli Federico, Capriati Michele

Academic Year: 2023-2024

Contents

1 | Introduction

1.1. Entry flows physics

One of the most critical phases of a space mission is the one during which a space vehicle has to go through the atmosphere of a celestial body. The flow around the vehicle is characterised by very high speeds; this emphasises the interactions between aerodynamics forces, thermal effects and chemical reactions. These interactions are the main interest of aerothermochemistry, a multidisciplinary field that involves fluid dynamics, thermodynamics and chemistry. It describes how chemical reactions and thermal effects affect the behaviour of gases in high-speed environments.
In the last 60 years humanity has successfully performed many entry mission to celestial bodies, [10] [42] [25], nonetheless our knowledge of the field around space vehicles is still limited.
Space vehicles can either be designed to survive an entry phase or can exploit it to disintegrate; the kinetic energy to be dissipated during this phase is in fact really large. Vehicles that want to get through an entry phase are typically designed with a blunt nose. This favors the detachment of the shock wave in front of the vehicle distancing the surface from the hottest region in the field, the one directly downstream the shock where the kinetic energy is transferred into thermal one. The temperature reached can be so high that atoms starts to dissociate and eventually ionize. In case this happens, radiation can also contribute to the heat flux experienced by the vehicle. Atoms start then to recombine cooling down in a region called thermal boundary layer. The residence time is typically not long enough for all the species to recombine and the remaining atoms chemically interact with the surface. The direct interactions between the surface and the flow occurring inside the boundary layer are characterised by heat and mass exchange.
Endothermic reactions occurring after the shock contribute to reduce the heat flux. Nonetheless, its value is typically so large that a thermal protection system is needed, if a space vehicle is designed to reach its final destination without disintegrating.
Thermal protection can be classified into two broad categories: ablative and reusable.
As the name suggests, reusable systems can withstand several entry missions. They are

typically made of ceramic materials arranged in tiles or layers. Heat dissipation is achieved mainly through re-radiation. To achieve that, materials characterised by high emissivity, low catalytic and low thermal conductivity are preferred. One of the most famous example of re-usable thermal protection system is the shield of the space shuttle made of carbon-carbon composites [9]. Reusable shields have the advantage of being able to withstand more than one entry mission, but the heat flux they can dissipate limit their range of application only to low-orbital entry missions.
Ablative materials can typically withstand a single entry mission. They are generally made of carbon fibers immersed in a phenolic resin. The heated material degrades into char and pyrolysis gases. Char experiences also ablation from chemical reactions and mechanical removal. The ablation products, combined with the pyrolysis gases, blow outside creating a layer that acts as a barrier against the heat.
As it has been said, the flowfield around an entry space vehicle is characterised by several complex physical and chemical process. Thus, it is important to be able to correctly duplicate the flight conditions of an entry mission so as to be able to study it in a controlled environment.

1.2. Experimental characterisation of Thermal Protection Systems

Experiments help scientists better understand the physical processes they are trying to replicate or simulate and they are of paramount importance when it comes to building models that try to describe the world around us. The environment and the conditions developing around a re-entry vehicle make it hard to perform controlled in-flight experiments, but starting with the Apollo missions 1972 data from re-entry missions have been collected and have helped scientists better understand the physics of atmospheric entry flows.
Ground testing tries to replicate in a controlled environment some of the critical aspects of the flight conditions; in the case of entry mission, the multiplicity of correlated physical phenomena makes it hard to find a common scaling that would allow one to test high velocity and high temperature effects at the same time. What is typically done then is to study the effects separately. The aerodynamics forces generated in high flight speed condition are studied in low enthalpy hypersonic wind tunnel, an example of them being the VKI Longshot [33], a wind tunnel located in the von Karman Institute (VKI), located in Sint-Genesius Rode, Belgium. These facilities can reach large Mach numbers (20 in the case of the VKI Longshot), but can only have short testing times and the enthalpy of

the gas is pretty low.
Then, to complement this first type of experiments, high enthalpy low speed experiments are performed. In these experiments one can replicate the heat loads experienced during entry mission duplicating the total enthalpy experienced in flight, the stagnation pressure and the velocity gradient. In the case of high speed, low enthalpy experiments, the parameters of the experimental setup are adjusted so as to duplicate the in flight Mach and Reynolds number, whereas during high enthalpy low speed experiments, it is relevant to duplicate the Damköhler number (quantifying the ratio between flow and chemical characteristic times); this number is a measure of how close the flowfield is to the chemical equilibrium. The larger the Damköhler number, the closer the flowfield to a chemical equilibrium condition; for Damköhler numbers smaller than one the chemistry of the flow can be considered frozen, whereas non-equilibrium phenomena are relevant when these numbers are close to the unit. Experiments have the advantage of replicating all the physics involved and all the coupled effects, but there is always some uncertainties associated with the measurements and, most importantly, they are rather time consuming. For this reason numerical simulations are also performed. Medium to low fidelity simulation tools allows in fact for a rather quick simulation of several flight conditions. They introduce a different type of uncertainties in the simulation given that the models used are typically characterised by empiric coefficients or parameters whose knowledge is almost always imperfect. These uncertainties, that one can refer to as model uncertainties are typically larger than the experimental ones.
As in many other fields the two approaches are complementary and they are used in combination; experiments are used to calibrate and validate numerical models that are used to quickly simulate a large number of relevant configurations. The value of experiments is not limited to the tuning of models, given that, as said, only experiments are able to replicate all the physics involved in certain flight conditions.
Uncertainty quantification (UQ) techniques play an important in the characterisation of Thermal Protection System (TPS). The main technique used in this work is the Forward Propagation of uncertainties. It can be simply thought of as a technique that tries to understand how the uncertainties on the input of a model or a function affect the uncertainties on the output of the model (or function) itself. In the framework of this thesis this technique has been used to propagate experimental and numerical uncertainties of two nitrogen-carbon ablation models.
The propagation of the uncertainties typically requires the simulation of a large number of experimental conditions. Although significantly faster than actually performing the experiment, numerically simulate hundreds or thousands of different conditions can be rather cumbersome. That is why one would be interested in building an approximation of

the numerical solver that allows an even quicker propagation of the conditions to simulate; this model is typically called surrogate model.
The objective of this thesis lies at the point of contact between the experimental characterisation of thermal protection system, the propagation of model uncertainties and the design of accurate surrogate models for high dimensional spaces.

1.3. Objectives and outline of the thesis

Although most of the atmospheric (re-)entry missions are missions in Earth's atmosphere, there is growing interest in the scientific community in the characterisation of the interactions between nitrogen and materials for TPS's. For example, NASA is planning for 2028 a mission on Titan [21], a moon of Saturn, whose atmosphere is about 98.4% nitrogen. Given that the main goal of the mission is the deployment of a robotic rotorcraft over the surface of this celestial body, there is interest in better understanding the gas-surface phenomena occurring in atmosphere that are dense in nitrogen.
The work performed in this thesis has precisely the objective of improving the understanding of the interactions between flows rich of this gas and graphite-based thermal protection systems; the primary objective of this work is the validation of the nitrogen-carbon ACA ablation model in the version proposed by Capriati [7] . This model is a Finite Rate Chemistry ablation model that has been calibrated with a Markov Chain Monte Carlo process. This process is a stochastic technique that has used the experimental results of a testing campaign in the VKI Plasmatron, a high-enthalpy plasma wind tunnel operated by the von Karman Institute [4], in conjunction with molecular beam experiments of Prata [31] to obtain the probability distribution functions of 10 model parameters describing the interactions between nitrogen flow and carbon-based TPS's. These parameters are coefficients of the differential equations describing the chemical production rates of the chemical species at the surface.
The validation of the model consists in the propagation of model and experimental uncertainties for a new testing campaign conducted in the Plasmatron. This new campaign is at higher pressures with respect to the one that has been used for the stochastic calibration (200 hPa for the new campaign, 15 hPa for the campaign used for the calibration).
Alongside the validation process, a comparison between the gas-surface interaction (GSI) models proposed by Capriati and the one proposed by Prata based on his experiments is presented.
The two models are different for the values of the coefficients in the chemical production rates equations; the same set of reactions and the same modelisation is considered.
The thesis is organised as follows:

1. **Chapter One** has introduced the the challenging topic of (re-)entry flows and has outlined the objectives of this work.
2. **Chapter Two** is dedicated to the modelling of the physics involved in (re-)entry problems. It introduces the governing equations of chemically reacting flows, the set of Navier-Stokes equations used for numerical simulations and the set of equations describing Gas-Surface interactions. The experimental facility is presented with its correlated setup and rebuilding techniques.
3. **Chapter Three** introduces the uncertainty quantification tools and techniques used in this work. More in particular, attention is given to forward propagation and sensitivity analysis techniques before presenting two types of surrogate models (Kriging and neural network) used in place of the full numerical solver.
4. **Chapter Four** presents a review and a deterministic simulation of the low pressure (15 hPa) experimental campaign used by Capriati for the calibration of his model. The experimental data of the second experimental campaign (100 hPa, 200 hPa) are also analysed.
5. **Chapter Five** is dedicated to the propagation of the uncertainties of the two model presented. In the first part, the second experimental campaign is simulated with both versions of the ACA model propagating the experimental uncertainties. The second part analyses the propagation of both experimental and model uncertainties in the Capriati's version of the model when simulating the experiments of the second campaign. A sensitivity analysis of the two models is also presented.
6. **Chapter Six** draws the conclusions of the work and suggests eventual future developments.

2 | Physical Modeling

The analyses performed in this work revolve around two experimental campaigns performed in the Plasmatron facility of the von Karaman Institute. A brief presentation of this unique facility is given in the first part of this chapter, before introducing the numerical rebuilding techniques used to recover the non-measured quantities. The second part of the chapter is dedicated to the physical models used to describe the interactions between the plasma flows and samples to be tested in the Plasmatron; these models constitute the base of the numerical simulation codes used to simulate the two experimental campaigns.

2.1. Experimental characterization

The two testing campaign whose results are used in the course of this work have been performed in the Plasmatron facility of the von Karman Institute.
It is an Inductively Coupled Plasma (ICP) facility typically used to perform high-enthalpy experiments. ICP facilities are used alongside arc-jets ones to test precise trajectory points. Measured quantities in both cases are typically the heat fluxes or the recession rates. Tests in ICP facilities can be run for a relatively long time, but they are rather inefficient when it comes to testing a full flight trajectory. In this case, CFD simulations are a better option given that they can simulate more cost-efficiently different trajectory points.
ICP facilities use electromagnetic fields to generate plasma. Gas is ionized using a radio frequency (RF) electromagnetic field.
On the other hand, arc jet wind tunnels generate high-temperature, high-speed gas flows using an electrical arc. Compared to ICP facilities they can reach higher temperatures and speeds, but the testing time is typically lower.
A more detailed description of the Plasmatron facility is given below.

2.1.1. The VKI Plasmatron facility

The VKI Plasmatron facility is an ICP plasma wind tunnel of the von Karman Institute used to perform high enthalpy experiments. It can duplicate the stagnation-point heat flux and recession experienced by an object traveling at hypersonic speed using a subsonic flow, following the procedure explained by Kolesnikov [13]. This ensures that the experiments can replicate the flight trajectory points of interest.
The Plasmatron can generate a highly pure and stable high enthalpy jet by means of a 160 mm diameter torch powered by a high-frequency, high-power, high-voltage (400 kHz, 1.2 MW, 2 kV) generator.
Initially, argon is injected, and once stabilised, the gas is switched to the desired one, nitrogen in the case of the experiments considered in this work.
Vacuum pumps are used to maintain the desired pressure.
The heat fluxes are measured by means of copper calorimeters whose temperature is kept stable at around 350 K thanks to a flow of water. Known the water mass flow and the difference of temperatures at the entrance and at the exit of the calorimeter water channel, it is possible to retrieve the heat flux. Temperatures are measured with two type-E thermocouples.
The sample is kept on the centreline of the plasma jet.
The already characterised uncertainties of the measurements in the Plasmatron are the folllowing:

1. Heat flux is known with a 10% accuracy
2. Both static and dynamic pressure are known up to a 0.25% accuracy
3. Plasma mass flow rate is known with a 5% accuracy

All these measurements are inputs of the flow rebuilding procedure that has been developed at VKI; it is described in Section 2.1.3. A detailed description of the experimental setup for the two testing campaign is given next.

2.1.2. Experimental setup

The Plasmatron is equipped with a 160 mm diameter ICP torch powered by a high-frequency, high-power, high-voltage (400 kHz, 1.2 MW, 2 kV) generator. The gas is heated by induction through a coil, providing a high purity plasma flow. The graphite test samples are 25 mm radius hemispheres with a 25 mm afterbody, machined in house at the von Karman Institute. Two different grains of raw graphite have been tested, the first being a superfine grain, and the second one being a high strength, wear resistant

graphite; both materials have been purchased from the company Graphtek LLC. In the course of this work, the tests on sample machined with the first grain contain in their name the lettering G_1, whereas tests performed on samples machined with the second grain type contain the lettering G_8.
The total stagnation point recession has been measured using a digital camera (Nikon D5000) attached to a 400 mm lens, giving a resolution of about 0.03 mm per pixel.
Samples are pre-heated by the argon plasma, before switching the test gas to pure nitrogen.
The facility is also equipped with an Acton Series SP-2750 spectrograph of 75 cm that can detect the strong radiative signature of the CN molecule. This molecule emits in the ultraviolet region (the most prominent emission band at around 388 nm). Objective of the spectral measurements is the determination of the locally resolved CN emission. CN emissions are used for tracking the material recession along with the chemistry in the reactive boundary layer as described in [18].
Experiments are typically characterised by a really low surface recession rate; this allows averaging several recorded spectra per ablation test.
The spectral measurement devices are calibrated by placing a tungsten ribbon lamp (OSRAM WI 17G) in the focus of the collection optics inside the test chamber.
Additionally, infrared thermography can be used to obtain 3D temperature maps of the sample.
These measurements, alongside the power supplied by the generator and its efficiency, are the inputs of numerical rebuilding techniques developed at VKI whose outputs are used in the ablative codes that simulates the gas-surface interaction. These techniques are briefly presented in the next section.

2.1.3. Numerical rebuilding techniques

The simulations of the experimental campaigns presented in this work are performed with the computational tool developed at the von Karman Institute by Munafò [29], named Stagline.
The simulations of the experiments requires as boundary conditions the conditions at the edge of the boundary in terms of pressure, temperature and velocity alongside the wall temperature at the surface. As already mentioned in Section 2.1.2, wall temperature, dynamic and static pressures are measured with a known uncertainty, whereas the edge temperature is retrieved by means of a numerical rebuilding technique.
The measured quantities and the power supplied to the generator are the inputs of the

procedure. First, the VKI ICP code [5] [1] [11] [35] is used to simulate the Plasmatron torch and the test chamber by solving magneto-dynamic equations, under the Local Thermodynamic Equilibrium (LTE) assumption. The conditions at the edge of the boundary layer are then known. The VKI BL code [3] is consequently used to simulate the flow inside the chemically reacting boundary layer to compute the heat flux on the probe, assuming it to be catalytic. An iterative process is used to compute the edge temperature with the convergence being reached once the measured heat flux and the one obtained in the simulations do match.
The rebuilding techniques allow one to obtain the velocity and the temperature at the edge of the boundary layer. They are both used as boundary conditions of the Stagline tool; the next section reviews the equations describing the physics of chemically reacting flows and the ones describing the gas-surface interactions that are solved inside Stagline.

2.2. Governing Equations

The next few Sections summarise the equations describing the physics of chemically reacting flows and the gas-surface interactions phenomena. First, a general review of the Navier-Stokes equations for chemically reacting flows in the continuum regime is given. The assumptions considered valid are the following:

1. Continuum regime
2. Thermal equilibrium
3. Chemical non-equilibrium
4. Unmagnatised plasma
5. Laminar flow
6. Radiative phenomena are negligible

These conditions hold because the Knudsen number, ratio between the mean free path and the characteristic length of the flow, is around the unit value; from that the continuum regime. The high temperatures expected (~10000 K for the edge temperature) and the low pressures the experiments have been run at (15-200 hPa) prevent the equilibrium of macroscopic quantities. High temperatures suggest the use of a multicomponent description of the flow given that high temperatures promote dissociation and ionisation phenomena. Low residence times suggest a departure from equilibrium that can be quantified computing the Dämkholer number, the ratio between the flow residence time and

the characteristic time of the chemistry. A Dämkholer number close to unity suggests that a finite rate description of the chemistry is needed. Lower values of the Dämkholer number are signs of strong departure from equilibrium conditions that may be assessed considering multi-temperature models; such models consider different temperatures for the vibrational, rotational, translational and electronic modes . Even stronger departures from equilibrium requires the adoption of more complex state-to-state approaches, that solve multiple continuity equations given that particles are grouped in pseudo-species based on their energy levels. In this work a neutral plasma is considered, meaning that the net charge of the flow is considered zero, even though free electrons are considered in the species. The plasma is also considered unmagnetised. The flow is expected to be laminar given that high temperatures flows are characterised by high viscosity. For this reason, the ratio between inertial and viscous forces, broadly known as Reynolds number, is expected to be low and with that the flow can be considered laminar.
Section 2.2.4 introduces a reduction of the Navier-Stokes equations simplified to describe the flow following the stagnation line only. The models needed for the closure of the equations are then presented, followed by a review of the finite rate description of gas-surface interaction phenomena. The chemically reactive atoms resulting from the ionisation/dissociation processes diffuse towards the surface and interacts with it. Balances of mass and energy on reacting surfaces are then needed to describe the response of thermal protection system.

2.2.1. Multi-component chemically reacting Navier-Stokes equations

A conservative form of the multi-component chemically reacting Navier-stokes equations under the assumptions presented above follows. Detailed derivations can be found in [2] [30]:

$$\frac{\partial \rho_i}{\partial t} + \nabla \cdot (\rho_i \mathbf{u} + \mathbf{j_i}) = \dot{\omega}_i, \quad \forall i \in [1, .., n_s], \tag{2.1}$$

$$\frac{\partial \rho \mathbf{u}}{\partial t} + \nabla \cdot (\rho \mathbf{u} \otimes \mathbf{u} + p\bar{\bar{I}} - \bar{\bar{\tau}}) = \mathbf{0}, \tag{2.2}$$

$$\frac{\partial \rho E}{\partial t} + \nabla \cdot (\rho \mathbf{u} H - \bar{\bar{\tau}} \cdot \mathbf{u} + \mathbf{q}) = 0, \tag{2.3}$$

Equation 2.1 describes the evolution of the chemical composition in terms of partial densities, ρ_i. $\mathbf{u}$ is the mass averaged velocity, $\mathbf{j_i}$ represents the mass flux of the species due to diffusion and $\dot{\omega}_i$ is the chemical volumetric production or destruction of species. The number of species continuity equations to be solved is the same as the number of

species considered. A six species model is considered in this work: $[N, N^+, N_2, e-, C, CN]$. Average mixture velocity can be obtained as:

$$\rho\mathbf{u} = \sum_{i=1}^{n_s} \rho_i \mathbf{u}_i. \tag{2.4}$$

The diffusive flux $\mathbf{j}_i$ is the product of the partial density ρ_i and the diffusion velocity v_i whose derivation is given in Section 2.2.3. Conservation of the total mass is guaranteed summing up Equation 2.1 for all the species; one obtains:

$$\frac{\partial \rho}{\partial t} + \nabla \cdot \rho\mathbf{u} = 0, \tag{2.5}$$

which is the canonic form of the continuity equation.
An additional constraint comes form the total density. Summing up all partial densities should allow one to retrieve the total one.

$$\sum_{i=1}^{n_s} \rho_i = \rho. \tag{2.6}$$

Equation 2.2 describes the conservation of momentum. Symbol p represents the thermodynamic pressure of the mixture, whose expression is given in Section 2.2.2, whereas τ is the viscous stress tensor; the expression for this tensor reads:

$$\bar{\bar{\tau}} = 2\mu D = \mu \left[\nabla\mathbf{u} + (\nabla\mathbf{u})^T - \frac{2}{3}\nabla \cdot \mathbf{u}\bar{\bar{I}} \right]. \tag{2.7}$$

No external forces acting on the elementary volume are considered in this work.
The conservation of total energy is expressed through Equation 2.3. Expression of the total energy is:

$$E = e + \frac{\mathbf{u}^2}{2}, \tag{2.8}$$

whereas the total enthalpy H can be retrieved as:

$$H = E + \frac{p}{\rho}. \tag{2.9}$$

The total heat flux across the fluid element boundaries is $\mathbf{q}$. Neglecting any radioactive components, it reads:

$$\mathbf{q} = -\lambda\nabla T + \sum_{i=1}^{n_s} \mathbf{j_i} h_i, \tag{2.10}$$

where λ is the gas thermal conductivity and h_i the specific enthalpy of species i. The term $\bar{\bar{\tau}} \cdot \mathbf{u}$ expresses the work of viscous stresses.

2.2.2. Multi-component thermodynamics

The properties of a mixture can be obtained averaging the properties of the single species. More in particular, one can write:

$$e = \sum_{i=1}^{n_s} Y_i e_i, \tag{2.11}$$

$$h = e + \frac{p}{\rho} = \sum_{i=1}^{n_s} Y_i h_i \tag{2.12}$$

$$c_{p,fr} = \sum_{i=1}^{n_s} Y_i c_{p,i} = \sum_{i=1}^{n_s} Y_i \left(\frac{\partial h_i}{\partial T}\right)_p, \tag{2.13}$$

$$s = \sum_{i=1}^{n_s} Y_i s_i - \frac{n k_B}{\rho} \sum_{i=1}^{n_s} X_i ln X_i, \tag{2.14}$$

$$g = \sum_{i=1}^{n_s} Y_i g_i - \frac{n k_B T}{\rho} \sum_{i=1}^{n_s} X_i ln X_i, \tag{2.15}$$

$$\tag{2.16}$$

where e_i, s_i, h_i, $c_{p,i}$, represents the species' internal energy, entropy, enthalpy and specific heat at constant pressure; Y_i represents the mass fraction of species i ($= \frac{\rho_i}{\rho}$), whereas $X_i = \frac{p_i}{p}$ is the molar fraction. One can see that entropy and Gibbs free energy are not simple averages given that an additional term has to be considered coming from the mixture's mixing entropy. The Boltzmann constant is represented as k_B. Finally, the frozen mixture specific heat at constant pressure is written as $c_{p,fr}$.
Expression for the species' internal energy, entropy, enthalpy, specific heat at constant pressure and partial pressure still need to be specified.
Particles store energy in four different modes:

1. Translational mode: kinetic energy stemming from the motion of the center of gravity of the particles. Particles have three degrees of freedom in the translational mode.

2. Rotational mode: kinetic energy related to the rotation around the axis of inertia. The number of degrees of freedom is highly dependent on the structure of the particle.

3. Vibrational mode: potential and kinetic energy coming from the vibration of the particles.
4. Electronic mode: potential and kinetic energy stemming from the rotations of the electrons in a specific shell.

Associating e_i^{tr}, e_i^r, e_i^v, e_i^{el} to translational, rotational, vibrational, electronic modes respectively, one can obtain the total internal energy as the sum of all these modes with the formation energy e^0:

$$e_i = e_i^{tr} + e_i^r + e_i^v + e_i^{el} + e_i^0 \tag{2.17}$$

The formation energy e^0 is defined as the enthalpy adsorbed or released upon the formation of one mole of substance from its constituent elements, at standard conditions. The contributions to the total internal energy of atoms come only from internal and electronic modes.
The internal energy and the other thermodynamic properties (constant pressure specific heat, specific entalphy and entropy) of the various species can be computed by means of models or exploiting the NASA polynomial approximation of thermodynamic properties [26]; NASA polynomials are analytical linear models with respect to temperature that approximates the quantities of interest. They are valid in a specific range of temperatures. An example of a model used to compute the thermodynamic properties is the Rigid Rotor Harmonic Oscillator (RRHO); its formulation can be found in [30], [41]. All properties can be obtained once the partition functions Q_i of species i is obtained. The partition function Q_i is the total partition function, obtained as the product of partition functions associated to translational, rotational, vibrational and electronic modes. One should ideally associate a different temperature to each energy mode; in this work each temperature is considered to be equal (thermal equilibrium).
Multi-temperature models consider different temperatures for the different modes. One broadly used model is the Park two-temperature model that considers two temperatures:

$$T^{tr} = T^r \tag{2.18}$$

$$T^{el} = T^v \tag{2.19}$$

On the other hand, the polynomial approximation of the thermodynamic properties is considered to be valid in the range 200-20000 K. Starting from the expression of the specific heat at constant pressure:

$$\frac{c_{p,i}}{R_i} = a_{0i}T^{-2} + a_{1i}T^{-1} + a_{2i} + a_{3i}T + a_{04}T^2 + a_{5i}T^3 + a_{6i}T^4, \tag{2.20}$$

one can integrate it in T to obtain the expressions for the enthalpy. The integration of Equation 2.20 divided by T in the same variable leads to the expression for the entropy:

$$\frac{h_i}{R_i T} = -a_{0i}T^{-2} + a_{1i}\frac{lnT}{T} + a_{2i} + a_{3i}\frac{T}{2} + a_{4i}\frac{T^2}{3} + a_{5i}\frac{T^3}{4} + a_{6i}\frac{T^4}{5} + \frac{a_{7i}}{T}, \tag{2.21}$$

$$\frac{s_i}{R_i T} = -a_{0i}\frac{T^{-2}}{2} - \frac{a_{1i}}{T} + a_{2i}lnT + a_{3i}T + a_{4i}\frac{T^2}{2} + a_{5i}\frac{T^3}{3} + a_{6i}\frac{T^4}{4} + a_{8i}. \tag{2.22}$$

$$\tag{2.23}$$

The expression for the internal energy can be obtained considering the expression linking it with the enthalpy:

$$e = h - RT. \tag{2.24}$$

It is in fact considered that the ideal law of ideal gases holds true.
Having seen how the thermodynamics properties are obtained, it is important to understand how some of the still unclosed terms in the Navier Stokes equations are modeled.

2.2.3. Multi-component Transport Equations

This section presents the models used to calculate the quantities whose expressions are needed to solve the set of Equations 2.1-2.3. These quantities are the diffusive mass fluxes j_i, the total thermal conductivity λ_i and the viscosity μ.
The single species viscosity and translational thermal conductivity can be obtained from the Chapman-Enskog first order expansion of the Boltzmann equation. Complete derivation can be found in [8]:

$$\mu_i = \frac{5}{16}\frac{\sqrt{\pi m_i k_B T}}{\bar{Q}_{ii}^{2,2}}, \tag{2.25}$$

$$\lambda_i^T = \frac{15}{4}R_i\mu_i, \tag{2.26}$$

$$\tag{2.27}$$

where $\bar{Q}_{i,j}^{(l,s)}$ is the collision integral. The quantities (l, s) represent the order of the Sonine polynomial used in the Chapman-Enskog expansion method.
From the same expansion one can also obtain the binary diffusion coefficient of species i in species j, that can be useful to compute the diffusion fluxes:

$$D_{ij} = \frac{3}{16n\bar{Q}_{ij}^{(1,1)}}\sqrt{\frac{2\pi k_B T(m_i + m_j)}{m_i m_j}}. \tag{2.28}$$

Diffusion velocities can be obtained solving the *Stefan-Maxwell* [39] system:

$$\sum_{i=1}^{n_s} G^V_{i,j}\mathbf{V}_i = -\frac{p}{nk_BT}\nabla X_i, \tag{2.29}$$

$$\sum_{i=1}^{n_s} Y_i\mathbf{V}_i = 0. \tag{2.30}$$

In the first equation the matrix $G^{\mathbf{v}}$ represents the diffusion matrix. The second equation expresses a mass constraint.
Diffusive fluxes are then obtained as:

$$\mathbf{J}_i = \rho_i\mathbf{V}_i \tag{2.31}$$

One could also obtain obtain the diffusive fluxes from Fick's law. First one obtains the effective binary diffusion coefficients given the binary diffusion coefficients:

$$D_i = \frac{1 - X_i}{\sum_{j\neq i}\frac{X_j}{D_{ij}}}, \tag{2.32}$$

then one can write the diffusive fluxes as:

$$\mathbf{J}_i = -\frac{pM_i}{RT}D_i\nabla X_i + Y_i\sum_{l=1}^{n_s}\frac{pM_l}{RT}D_l\nabla X_l \tag{2.33}$$

Finally one can obtain the multicomponent version of the coefficients whose derivation has been obtained above.
The multi-component mixture coefficients $\tau = [\mu, \lambda^T]$ are obtained as follows:

$$\tau = \sum_{i=1}^{n_s}\alpha_i^\tau X_i, \tag{2.34}$$

with coefficients α_i^τ obtained from the solution of the system:

$$\mathbf{G}^\tau\alpha^\tau = [X_1, .., X_{n_s}]^T. \tag{2.35}$$

The expression of $\mathbf{G}$ can be found in A. The multi-component expression of the thermal conductivity can be obtained from the summation of internal, thermal and electronic conductivity.

Viscosity of the gas mixture is given by the viscosities of the pure species mixed according

to the mixing rule of Herning and Zipperer [15],

$$\mu = \sum_{i=1}^{n_s} \frac{\mu_i y_i}{\phi_i}, \qquad \phi_i = \sum_{j \neq i} y_j \sqrt{\frac{M_j}{M_i}}. \tag{2.36}$$

The thermal conductivity of the mixture is obtained from the expression of the viscosity of the mixture itself.

$$\lambda = \frac{c_p \mu}{Pr} \tag{2.37}$$

$$D_i = D = \frac{\mu}{\rho Sc}, \tag{2.38}$$

The symbols Pr and Sc represent the Prandtl and the Schmidt number respectively. The Schmidt number express the ratio between the viscous and mass diffusion rate, obtained as:

$$Sc = \frac{\mu}{\rho D} \tag{2.39}$$

The Prandtl number expresses the ratio between the cinematic and thermal diffusivity:

$$Pr = \frac{\mu c_p}{\lambda} \tag{2.40}$$

2.2.4. Stagnation-line reduced Navier-Stokes Equations

In this section the dimensionally reduced Navier-Stokes equations (DRNSE) proposed by Klomfass and Múller [17] are briefly presented. In this approach the governing set of Equations 2.1-2.3 are simplified by reducing the number of independent spatial variables, leading to a quasi one-dimensional approximation for the stagnation streamline. The dimensionality reduction allows for faster computation and it is especially interesting when evaluating the effects of finite-rate chemistry on the convective stagnation-point heating of re-entry vehicles or planetary probes. The original set of chemically reacting Navier-Stokes Equations (Eq. 2.1-2.3) is written in spherical coordinates (r, θ, ϕ) considering a rotationally symmetric flow problem. Considering the symmetry of the problem, introducing the separation of variable:

$$\mathbf{f}\,(r, \theta) = \mathbf{f}_1(\theta)\mathbf{f}_2(r), \tag{2.41}$$

and considering valid the Newtonian theory providing the approximation:

$$p_w - p_\infty = \rho_\infty u_\infty^2 cos^2\theta, \tag{2.42}$$

the following relations describe the variability of the quantities of interest:

$$u_r = \overline{u}_r(r)cos\theta, \tag{2.43}$$

$$u_\theta = \overline{u}_\theta(r)sin\theta, \tag{2.44}$$

$$p = p_\infty + \overline{p}(r)cos^2\theta, \tag{2.45}$$

$$T = \overline{T}(r), \tag{2.46}$$

$$X_i = \overline{X}_i(r). \tag{2.47}$$

The subscripts (r, θ, ϕ) describe the components of the quantity along one of the three directions.

Equations 2.43-2.47 are then inserted into Equations 2.1-2.3 , re-written in spherical coordinates; given that the interest is for the stagnation line quantities, the limit $\lim_{\theta\to 0}$ is considered.
This limiting process returns:

$$\frac{\partial \mathbf{U}}{\partial t} + \frac{\partial \mathbf{F}^c}{\partial t} + \frac{\partial \mathbf{F}^d}{\partial t} = \mathbf{S}^c + \mathbf{S}^d + \mathbf{S}^k, \tag{2.48}$$

where $\mathbf{U}$ is the conservative variable, $\mathbf{F}^c, \mathbf{F}^d$ are the conservative and diffusive fluxes:

$$\overline{\mathbf{U}} = \begin{bmatrix} \rho_1 \\ \vdots \\ \rho_{n_s} \\ \rho\overline{u}_r \\ \rho\overline{u}_\theta \\ \rho E \end{bmatrix}, \quad \overline{\mathbf{F}}^c \begin{bmatrix} \rho_1\overline{u}_r \\ \vdots \\ \rho_{n_s}\overline{u}_r \\ \rho\overline{u}_r^2 + p \\ \rho\overline{u}_r\overline{u}_\theta \\ \rho\overline{u}_r H \end{bmatrix}, \quad \overline{\mathbf{F}}^d = \begin{bmatrix} J_{r1} \\ \vdots \\ J_{rs} \\ -\tau_{rr} \\ -\tau_{r\theta} \\ -\tau_{rr}u_r \end{bmatrix}. \tag{2.49}$$

The total energy term writes:

$$\rho E = \sum_{i=1}^{n_s} \rho_i e_i + \rho\frac{u_r^2}{2}. \tag{2.50}$$

Total enthalpy H is defined as:

$$H = E + \frac{p}{\rho}. \tag{2.51}$$

The terms $\mathbf{S}^c$ and $\mathbf{S}^d$ are convective and diffusive source terms:

$$\mathbf{S}^c = -\frac{(u_r + u_\theta)}{r}\begin{bmatrix} 2\rho_1 \\ \vdots \\ 2\rho_{n_s} \\ 2\rho u_r \\ 3\rho u_\theta - 2\frac{p-p_\infty}{u_r+u_\infty} \\ 2\rho H \end{bmatrix}, \qquad \mathbf{S}^d = -\frac{1}{r}\begin{bmatrix} 2J_{r1} \\ \vdots \\ 2J_{rn_s} \\ 2(\tau_{\theta\theta} - \tau_{rr} + \tau_{r\theta}) \\ \tau_{\theta\theta} - 3\tau_{r\theta} \\ 2(\tau_{rr}u_r - \tau_{r\theta}u_r - \tau_{\theta\theta}u_\theta) \end{bmatrix}. \quad (2.52)$$

The radial species diffusion J_{ri} are obtained by solving the approximate Stefan-Maxwell equation following an approach similar to the one presented in Section 2.2.3.
The components of the stress tensor in the system are the following:

$$\tau_{rr} = \frac{4}{3}\eta\left(\frac{\partial u_r}{\partial r} - \frac{u_r + u_\theta}{r}\right), \qquad \tau_{r\theta} = \eta\left(\frac{\partial u_\theta}{\partial r} - \frac{u_r + u_\theta}{r}\right), \quad \tau_{\theta\theta} = -\frac{1}{2}\tau_{rr}. \quad (2.53)$$

The symbol η represents the shear viscosity.
Finally, the term, $\mathbf{S}^k$ represents the internal kinetic and energy transfer term vector:

$$\mathbf{S}^k = \begin{bmatrix} \dot{\omega}_1 \\ \vdots \\ \dot{\omega}_{n_s} \\ 0 \\ 0 \\ 0 \end{bmatrix} \quad (2.54)$$

The terms $\dot{\omega}_i$ are the mass production rates.
Calling $\mathcal{R}$ the set of equations used to describe the chemistry considered, one can describe the kinetics of each elementary reaction r in the set through the following formula:

$$\sum\nolimits_{\mathrm{k}\in\mathcal{S}^*} \nu'_{\mathrm{kr}} \mathrm{A}_k \rightleftharpoons \sum\nolimits_{\mathrm{k}\in\mathrm{S}} \nu''_{\mathrm{kr}} \mathrm{A}_k, \quad (2.55)$$

$$(2.56)$$

where $\mathcal{S}^*$ represents the set containing all the species considered, the superscript $\cdot'$ indicates the forward reaction and the superscript $\cdot''$ indicates the backward one, the symbols ν_{kr} are the stoichiometric coefficients for species A_k in reaction r. The *Law of Mass Action* states that the production of a reaction product is proportional to the product of the reactant densities raised to their stoichiometric coefficients. The proportionality constant k_f does not depend on the reactant densities and is called the rate coefficient. Considering

that the subscript f indicates the forward reaction and the subscript b the backward one, one can express the molar rate-of-progress as:

$$\nu_{j,r}^{'} = k_{f,r} \prod_{j \in \mathcal{S}^*} \hat{\rho}_j^{\nu_{j,r}^{'}} - k_{b,r} \prod_{j \in \mathcal{S}^*} \hat{\rho}^{\nu_{j,r}^{'}} Z, \tag{2.57}$$

where symbol $\hat{\rho}_j = \frac{\rho_j}{M_j}$ is the molar density of species j.
The molar rate-of-progress for a reaction r can be written as:

$$\mathfrak{R}_r = k_{f,r} \prod_{j \in \mathcal{S}^* \hat{\rho}_j^{\nu_{jr}^{'}}} - k_{b,r} \prod_{j \in \mathcal{S}^* \hat{\rho}_j^{\nu_{jr}^{''}}} . \tag{2.58}$$

At equilibrium the rate of progress of all reactions is zero. The equilibrium constant, defined as the ratio between forward and backward reactions, yielding to the definition of the equilibrium constant $K_{eq,r}$:

$$K_{eq,r} = \frac{k_{f,r}}{k_{b,r}} = \prod_{j \in \mathcal{S}^*} (\hat{\rho}_j^*)^{\left(\nu_{jr}^{''} \nu_{jr}^{'}\right)}. \tag{2.59}$$

Exploiting Equation 2.57, one can write the total mass production rate for a single species k as:

$$\dot{\omega}_k = M_k \sum_{r \in \mathcal{R}} (\nu_{kr}^{''} - \nu_{kr}^{'}) \mathfrak{R}_r, \quad k \in \mathcal{S}^*. \tag{2.60}$$

One still has to define the reaction rates constants. One broadly used approach assumes they follow an Arrhenius law expressing a dependence on temperature. Their expression reads:

$$k_f(T) = A T^{\beta} \exp\left(-\frac{E_a}{R_u T}\right). \tag{2.61}$$

This type of expressions have to be tuned experimentally. Other approaches for the estimation of these coefficients have been derived from quantum mechanics considerations [40].
One should also consider third-body reactions, that is to say, reactions requiring an additional species to provide or remove energy from the reactants, remaining inert in the process. Generic third bodies are commonly denoted with a letter M. For example, heavy particle impact dissociation of the nitrogen molecule can occur by collision with different atoms:

$$\mathrm{N_2 + N} \rightleftharpoons \mathrm{N + N + N} \tag{2.62}$$

$$\mathrm{N_2 + O} \rightleftharpoons \mathrm{N + N + O} \tag{2.63}$$

The expression for a generic third heavy particle is then:

$$N_2 + M \rightleftharpoons N + N + M \tag{2.64}$$

The activation energy required in a given third body reaction is the same, regardless of which third body provides the energy. The net rate-of-progress for a third body reaction is then written as:

$$\mathfrak{R}_r = \left[k_{f,r} \prod_{j \in \mathcal{S}^*} \hat{\rho}_j^{\nu'_{jr}} - k_{b,r} \prod_{j \in \mathcal{S}^*} \hat{\rho}_j^{\nu''_{jr}} \right] \sum_{j \in \mathcal{S}^*} \alpha_{jr} \hat{\rho}_j \tag{2.65}$$

2.2.5. Finite Rate Gas Surface Interaction

The understanding of the interactions between the surface of the thermal protection system and the surrounding flow is crucial for an efficient design of reliable protection systems for space vehicles. In this section finite-rate gas-surface chemistry models are presented. During the course of this work the only types of reactions considered are ablative and catalytic one; neglected are other phenomena such as spallation, mechanical removal or pyrolisis.

The surface can either act as a catalyser favorising the recombination of the gas-atoms (catalytic reactions) or can itself be active part of the reactions occurring. For example, atoms of the surface can react with gas-phase ones. This can lead to a stream of molecules leaving the surface; the consequent stream of particles ablated away from the surface has a blowing velocity at the surface.

The material response is modeled in terms of surface mass and energy balances at the surface. The simplest way of expressing a balance for a conservative quantity $\mathbf{F}$ is the following:

$$[\mathbf{F}_g - \mathbf{F}_s] \cdot n = S_s \tag{2.66}$$

where the difference between the fluxes in and from the gas is inside brackets and the term S_s represents the surface source terms; $\mathbf{n}$ is the vector normal to the surface pointing away from it.

As explained in Section **??**, the temperature of the surface of the carbon samples is measured. For this reason, when simulating the testing campaigns in the Plasmatron, one can avoid solving the energy balance and only solve the mass one.

For the mass balance of each species one can write:

$$\dot{\omega}_i = (\rho(\mathbf{u}_g - \mathbf{u}_r) + \mathbf{j}_i) \cdot \mathbf{n}, \quad \forall i \in [1, ..., n_s] \tag{2.67}$$

The symbols $\mathbf{u}_g$, $\mathbf{u}_r$ are the advection and recession velocity, respectively. Their expressions can be obtained from the blowing mass rate $\dot{m} = \sum_{i=1}^{n_s} \dot{\omega}_i$:

$$\mathbf{u}_g = \frac{\dot{m}}{\rho}, \tag{2.68}$$

$$\mathbf{u}_r = \frac{\dot{m}}{\rho_s}. \tag{2.69}$$

The recession velocity can be neglected with respect to the blowing one in the mass balance equation being significantly smaller, obtaining:

$$\dot{\omega}_i = (\rho \mathbf{u}_g + \mathbf{j}_i) \cdot \mathbf{n}, \quad \forall i \in [1, ..., n_s] \tag{2.70}$$

The blowing mass rate is bigger than zero only when the surface is at least partly catalytic. The closure to the surface balance equation is obtained once the chemical production rate $\dot{\omega}_i$ for each species is known. Simple approaches for obtaining the chemical production rates are phenomenological ones. They are based on the definition of the probability that a macroscopic reaction at the surface takes place. The probability of reaction r is defined as:

$$\gamma_i^r = \frac{N_i^r}{N_i}, \tag{2.71}$$

with N_i^r being the number flux of species i subject to the reaction r, whereas N_i is the number flux of species i impinging the surface.
The number flux of species i impinging on the surface can be written as $N_i = n_i \sqrt{k_B T_s/(2\pi m_i)}$.
The species production rates can then be simply obtained as:

$$\dot{\omega}_i = m_i \gamma_i^r N_i. \tag{2.72}$$

The models of Prata and Capriati used in the course of this work are finite-rate chemistry models; these type of models describe each reaction occurring at the surface singularly. Chemical production rates are described as follows:

$$\dot{\omega}_i = M_i \sum_{r=1}^{n_r} \nu_{i,r} k_r \prod_{j \in S} \left(\frac{\rho_j}{M_j} \right)^{\nu_{j,r}} \tag{2.73}$$

Depending on the type of reaction described the form of the rate coefficient depends on the type of reaction considered. Surfaces are characterised by a total active site density B. Below are reported the different type of reactions considered and the associated form of the rate coefficient k_r. Symbol G refers to gas atoms, symbol s indicates a surface free

site and the subscript $\cdot_s$ is used for atoms absorbed by the surface.

1. *Adsorption of atoms*: $\mathrm{G} + \mathrm{s} \longrightarrow \mathrm{G}_s$
   The adsorption rates read:

$$k_{abs,i} = \frac{s}{B} V_{T,i} exp\left(-\frac{T_{abs,i}}{T}\right), \tag{2.74}$$

   where s, comprises between 0 and 1 is the selectivity of the adsorption, $V_{T,i} = \sqrt{\frac{k_B T}{2\pi m_i}}$ and $T_{abs,i}$ represents the activation energy of the adsorption reaction.

2. *Desorption of atoms*: $\mathrm{G}_s \longrightarrow \mathrm{G} + \mathrm{s}$
   The desorption rates read:

$$k_{des,i} = \frac{2\pi m_i k_B T^2}{N_A B h^4} exp\left(-\frac{T_{des,i}}{T}\right), \tag{2.75}$$

   where N_A is the Avogadro's constant, h is the Planck's constant and $T_{des,i}$ represents the activation energy of the desorption.

3. *Eley-Rideal (ER) absorption*: $\mathrm{G} + \mathrm{G}_s \longrightarrow \mathrm{M} + \mathrm{s}$
   This type of reaction occurs when a gas-phase atom recombines with and absorbed ones. The reaction rates reads:

$$k_{er,i} = \frac{1}{B} V_{T,i} \gamma_{er,i} exp\left(-\frac{T_{er,i}}{T}\right), \tag{2.76}$$

   where $\gamma_{er,i}$ is the probability of the ER reaction and $T_{er,i}$ is the activation energy of the reaction.

4. *Langmuir-Hinshelwood (LH) absorption*: $\mathrm{G}_s + \mathrm{G}_s \longrightarrow \mathrm{M} + \mathrm{s}$
   This reaction occurs when two absorbed atoms interact escaping the potential barrier of the surface.

$$k_{er,i} = \sqrt{\frac{N_A}{B}} V_{T,i} \gamma_{lh} exp\left(-\frac{T_{lh,i}}{T}\right), \tag{2.77}$$

   where $\gamma_{er,i}$ is the probability of the LH reaction.

5. *Gas dependent surface ablation*:
   Gas atoms can recombine with carbon atoms of the surface and then leave the surface. This leads to ablation of the surface. When this type of reaction is surface

dependent the rate coefficient writes:

$$k_{gd,i} = V_{T,i}\gamma_{gd}, \tag{2.78}$$

with γ_{gd} being the probability that this reaction takes place.

6. *Gas independent surface ablation*:
   When ablation reactions are gas-indipendent the rates coefficient has an Arrenhius-like formula:
$$k_{gi,i} = A_{gi,i}T^{n_{gi,i}}\exp(-\frac{T_{gi,i}}{T}), \tag{2.79}$$

Table 2.1 reports the set of reactions that are considered by the two versions of the ablation model. It consists of six reactions. The version proposed by Prata is a subset of the original Air Carbon Ablation model proposed by Prata himself that was composed of 20 reactions. The subset contains all the reactions involving nitrogen. In the version of the model proposed by Capriati, the same reactions with new values for the rate coefficients are considered. The symbol b indicates the bulk material.

	Reaction	Reaction Rate
1	$\mathrm{N} + \mathrm{s} \longrightarrow \mathrm{N}_s$	$k_1[N][s]$
2	$\mathrm{N}_s \longrightarrow \mathrm{N} + \mathrm{s}$	$k_2[N_s]$
3	$\mathrm{N} + \mathrm{N}_s + \mathrm{C}_b \longrightarrow \mathrm{CN} + \mathrm{N} + \mathrm{s}$	$k_3[N][N_s]$
4	$\mathrm{N} + \mathrm{N}_s \longrightarrow \mathrm{N}_2 + \mathrm{s}$	$k_4[N][N_s]$
5	$\mathrm{N}_s + \mathrm{N}_s \longrightarrow \mathrm{N}_2 + 2\,\mathrm{s}$	$k_5[N_s][N_s]$
6	$\mathrm{N}_s + \mathrm{C}_b \longrightarrow \mathrm{CN} + \mathrm{s}$	$k_6[N_s]$

Table 2.1: Set of surface reactions used in the Prata and Capriati models.

The Prata and Capriati's versions of the ACA model differ for the value of the reaction coefficient used. The rate coefficients for reaction r can be written in the form:

$$k_r = X_r exp\left(-\frac{E_r}{T_w}\right). \tag{2.80}$$

The symbol X_r represents a pre-exponential coefficient, whereas E_r is the activation energy.
Table 2.2 summarises the rate coefficients of the Prata model and the ones of Capriati. The rates proposed by Capriati are the results of a Markov Chain Monte Carlo processs; a distribution of the rates is then obtained. In the course of this work the mean values of the

distribution resulting from the MCMC are used when a deterministic value is considered for the Capriati's version of the model.

	Reaction	Prata model		Capriati model	
		X	E	X	E
1	$N + s \longrightarrow N_s$	1	2500	1	4.5386e+02
2	$N_s \longrightarrow N + s$	1	73971.6	1	73971.6
3	$N + N_s + C_b \longrightarrow CN + N + s$	1.5	7000.0	0.0165	1.4074e+03
4	$N + N_s \longrightarrow N_2 + s$	0.5	2000.0	0.0004771	1.1807e+04
5	$N_s + N_s \longrightarrow N_2 + 2\ _s$	0.1	21000.0	0.00047167	1.5459e+04
6	$N_s + C_b \longrightarrow CN + s$	1e+8	20676.0	796333122.4111	2.5375e+04

Table 2.2: Comparison between the rate coefficients of the Prata and Capriati models.

For completeness, here are also reported the value of the surface site density B:

$$B_{Prata} = 6.022e + 18 \qquad B_{Capriati} = 1.908e + 17 \tag{2.81}$$

For each chemical species it is possible to apply the law of mass action (see Section 2.2.4) to obtain a differential equation describing the chemical production. The set of equations reads:

$$\frac{d}{dt}[N] = -k_1[N][s] + k_2[N_s] - k_4[N][N_s] \tag{2.82}$$
$$\frac{d}{dt}[N_2] = k_4[N][N_s] + k_5[N_s]^2 \tag{2.83}$$
$$\frac{d}{dt}[CN] = k_3[N][N_s] + k_6[N_s] \tag{2.84}$$
$$\frac{d}{dt}[N_s] = k_1[N][s] - k_2[N_s] - k_3[N][N_s] - k_4[N][N_s] - 2k_5[N_s]^2 - k_6[N_s] \tag{2.85}$$

The unknowns of the problem are:

$$[N_s],\ [s],\ [N_s],\ \frac{d}{dt}[N_s],\ \frac{d}{dt}[N],\ \frac{d}{dt}[N_2],\ \frac{d}{dt}[CN] \tag{2.86}$$

Thus, two more equation are needed to solve the problem:

$$\frac{d[s]}{dt} = 0 \qquad B = [G_s] + [s] \tag{2.87}$$

The first equation is valid because we consider the solution at steady-state, while the

second describes the conservation of total number of active sites.

2.3. Stagnation line simulation tools

The main tool used in this work to simulate the experiments in the Plasmatron facility is the VKI Stagnation line code, a CFD developed at the von Karman Institute. It is coupled with the Mutation++ library that can be used for many purposes, including the computation of the thermodynamics properties, the chemistry and the resolution of the gas-surface interaction.

2.3.1. The Mutation++ Library

Mutation++ is a software library written in C++ language. According to his developer James B. Scoggings it has been developed with the following six goals in mind:

1. provide accurate thermodynamic, transport, and chemical kinetic properties for multicomponent, partially ionized gases,
2. ensure the efficient evaluation of these properties using state-of-the-art algorithms and data structures,
3. be easily extendable to incorporate new data or algorithms as they become available,
4. interface to any CFD tool through a consistent and logical interface,
5. use self-documenting database formats to decrease data transcription errors and increase readability, and
6. be open source to promote code and data sharing among different research groups.

It is composed of several modules:

- *Thermodynamics module:*
  it allows for the computation of the Thermodynamics properties of the gas mixtures using either the Rigid-Rotor and Harmonic Oscillator Model or the NASA Thermodynamic Polynomials database as it has been explained in Section 2.2.2.
- *Transport module:*
  it can compute viscosity, thermal conductivity, thermal diffusion ratios and diffusion velocities following the Chapman-Enskog expansion method and solving the Stefan-Maxwell Equation (see Section 2.2.3).
- *Chemical kinetics*:

its goal is the computation of species production rates according to a finite-rate description of chemical reactions as presented in Section 2.2.4.

Mutation++ can be interfaced with a CFD solver and returns the physico-chemical properties of a gas-mixture receiving as input the state vector **U**.

2.3.2. The VKI stagnation-line solver

The VKI stagnation line solver is a medium fidelity solver internally developed at VKI by Munafò. It is based on the dimensionally reduced Navier Stokes equation presented in Section 2.48.

The set of Equations 2.48 is spatially discretised using a Finite Volume (FV) scheme. It achieves second-order accuracy in space and it is integrated in time using the implicit Backward-Euler method. The local time step reads:

$$\Delta t_i = \frac{CFL\Delta r_i}{\left(|u_r| + c + \frac{1}{\Delta r} max(\frac{4}{3}\frac{\mu}{\rho}, \frac{\lambda}{c_v})\right)_i}, \tag{2.88}$$

where CFL is the Courant-Friedrichs-Lewy (CFL) number, c is the gas frozen speed of sound and c_v is the specific heat at constant volume.

Boundary conditions are imposed using variables at ghost-cells.

For the simulation of the experiments in Plasmatron constant temperature at the wall (Isothermal) is imposed; on top of that a steady-state ablation condition is considered. Neglecting pyrolysis, the species mass balance at the surface reads:

$$(\rho_i u_r)_w + (J_{ri})_w = \dot{\omega}_i \quad \forall i \in \mathcal{S}, \tag{2.89}$$

where the first two terms are the convective and diffusive mass fluxes of species i, while $\dot{\omega}_i$ represents the blowing rates of species i.

The closure for the species chemical production rates follows the procedure presented in Section 2.2.5.

The ablative boundary condition is closed with the addition of constraints at the wall:

$$(T)_w = T_w, \quad \left(\frac{\partial p}{\partial r}\right)_w, \quad (u_\theta)_w = 0, \tag{2.90}$$

where the subscripts $(\cdot)_w$ indicates that the variables are evaluated at the wall.

The code is fully coupled with the library Mutation++ that is used to compute the thermodynamics, the chemistry, transport properties and to solve the GSI boundary con-

ditions.

2.4. Summary

Following a brief presentation of the VKI Plasmatron Experimental setup and the rebuilding techniques used to obtain relevant quantities from the ones measured during the experiments, a brief recall to the physical models used to describe chemically reacting flows and gas-surface interactions has been given. The last part of this chapter has been dedicated to the presentation of the Stagnation line simulation tools; internally designed in VKI, they are based on the physical models described in the first part of the chapter and they allow for the analysis of gas-surface stagnation point interactions.

3 | Uncertainty quantification tools and techniques

This chapter introduces the Uncertainty Quantification techniques used in this work. At first, a technique called forward propagation is presented; it is used to quantify the uncertainties on the output of a model given the uncertainties on the inputs of the model itself. Then, sensitivity analysis techniques are briefly described. They are useful for understanding how much the variability of an output of a model is described by the variability of each inputs. Both the techniques above mentioned are computationally demanding requiring a lot realisations of the models to be analysed. Surrogate modelling techniques are therefore introduced in the second part of the chapter; these techniques drastically reduce the computational time required to obtain realisations of complex models, making the application of UQ techniques possible in a reasonable amount of time.

3.1. Forward propagation

Forward propagation of the uncertainties is a technique that allows one to understand how the uncertainties on the inputs of a model propagate through the model itself resulting in uncertainties on the output of the model. When uncertainties are present in the input space, one can associate this input space to a (multi-variate) random variable $\mathbf{X}$ and a joint probabilistic density function (PDF) $p(\mathbf{x})$. Calling the model $\mathcal{M}$, the resulting output is then: $\mathcal{Y} = \mathcal{M}(\mathbf{X})$. Typically one is interested in characterising the first and second statistical moment of $\mathcal{Y}$. These two moments represent the mean and the variance of the output; their analytical expression would read:

$$\mu_y = \mathbb{E}\left[\mathcal{M}(\mathbf{x})\right] = \int_{-\infty}^{+\infty} \mathcal{M}(\mathbf{x}) p(\mathbf{x}) d\mathbf{x}, \tag{3.1}$$

$$\sigma_y^2 = \mathbb{E}\left[\left(\mathcal{M}(\mathbf{x}) - \mathbb{E}\left[\mathcal{M}(\mathbf{x})\right]\right)^2\right] = \int_{-\infty}^{+\infty} \left(\mathcal{M}(\mathbf{x}) - \mathbb{E}\left[\mathcal{M}(\mathbf{x})\right]\right)^2 p(\mathbf{x}) d\mathbf{x}. \tag{3.2}$$

The operator $\mathbb{E}(\cdot)$ indicates the expected value of the quantity $(\cdot)$. The analytical calculation of the integrals 3.1, 3.2 is typically not feasible, thus numerical methods are usually exploited. The most direct numerical technique to solve for the mean and the variance is the Montecarlo (MC) simulation [28] consisting in an estimation of the quantities of interest (mean and variance) through the evaluation of a limited number of samples from the input space. Considering N_s samples drawn from the input space, the estimation of the mean and the variance is obtained as follows:

$$\tilde{\mu}_y = \frac{1}{N_s} \sum_{i=1}^{N_s} \mathcal{M}(\mathbf{x}_i) \tag{3.3}$$

$$\tilde{\sigma}_y^2 = \frac{1}{N_s} \sum_{i=1}^{N_s} \left(\mathcal{M}(\mathbf{x}_i) - \tilde{\mu}_y\right)^2 \tag{3.4}$$

According to the law of large number, the convergence of the estimators $\tilde{\mu}_y, \tilde{\sigma}_y^2$ to the actual values of the mean and variance of the output, μ_y and σ_y^2, given the PDF of the input $p(\mathbf{x})$ and the model $\mathcal{M}(\mathbf{X})$ when considering a large number of points N_s is guaranteed.

The convergence of the Montecarlo technique does not depend on the dimension of the method, making this technique really interesting for the estimation of the uncertainties of the output for models whose dimension is relatively large. On the other hand, it typically requires a large number of samples before obtaining a good convergence of the quantities of interest; its convergence rate is in fact $\mathcal{O}\left(\frac{1}{\sqrt{N_s}}\right)$. Techniques have been then developed to the fasten the rate of convergence. In this work, the latin lypercube sampling technique [27] is used. This technique aims at carefully selecting the location of the samples inside the input space so as to obtain a faster convergence of the MC sequence. In the case of one-dimensional hypercube sampling, the cumulative distribution function of the distribution from which the samples are drawn is evenly divided into N regions (when N is the number of samples to be drawn). One sample for each region is then randomly drawn. In the case of more than one-dimensional distributions to draw from, one-dimensional LHS samples are drawn for each dimensions according to the technique used for the one-dimensional case. Then, the LHS one-dimensional samples are randomly combined to form vectors of the right dimension.

3.2. Sensitivity analysis

Sensitivity analysis is an ensemble of techniques used to determine how the variability of independent variables of a model affect the variability of a dependent variable of the

same model. It is used to assess the impact of changes in input variables on the output of a model or system. One of the main goal of sensitivity analysis is the understanding of which independent variables mostly affect the variability of the output.
There are mainly two type of sensitivity analysis:

- *Local Sensitivity Analysis*:
  it examines how changes in single independent variables reflect in changes in the output. The analysis is typically performed varying one input at a time, whilst keeping all other inputs constant.
- *Global Sensitivity Analysis*:
  this second type of analysis studies simultaneously the variability of multiple input variables.

In the course of this work two type of sensitivity analysis study has been used. The first is a local one, called *One-at-a-Time (OAT) Analysis*; it is well suited when one is interested in seeing how each individual variable affects the output. Each input is varied while keeping the others constant and the effect on the output is observed. An overview of sensitivity analysis techniques, including the *One-at-a-Time (OAT) Analysis* can be found in [34]. The second one is the calculation of the Sobol Indices [37]. It is a global technique that allows one to understand the impact of the variability of the input variables on the variability of the output. In fact, the variance of the output is seen as the summation of contributes from each individual variable, called *indices*. This is a sort decomposition of the variance. Cross-effects between variables are considered in the calculation of higher order indices.
The decomposition is made possible by the fact that a function model $\mathcal{Y} = \mathcal{M}(\mathbf{x})$ can be decomposed as follows:

$$Y = \mathcal{M}_0 + \sum_{i=1}^{d} \mathcal{M}_i(x_i) + \sum_{i<j}^{d} \mathcal{M}_{ij}(x_i, x_j) + ... + \mathcal{M}_{1,2,...,d}(x_1, x_2, ..., x_d) \tag{3.5}$$

where d is the number of variables of the model considered, $\mathcal{M}_0$ is a constant, $\mathcal{M}_i$ is a function of X_i only, $\mathcal{M}_{ij}$ is a function of X_i, X_j. One can rewrite the various contributions of Equation 3.5 as:

$$\mathcal{M}_0 = \mathbb{E}(\mathcal{Y}), \quad \mathcal{M}_i(x_i) = \mathbb{E}(\mathcal{Y}|x_i) - \mathcal{M}_0, \quad \mathcal{M}_ij(x_i, x_j) = \mathbb{E}(\mathcal{Y}|x_i) - \mathcal{M}_0 - \mathcal{M}_i - \mathcal{M}_j, \tag{3.6}$$

then one may see that $\mathcal{M}_i$ is the effect of varying X_i, $\mathcal{M}_{ij}$ is the effect of varying x_i, x_j simultaneously (comprehensive of their individual variations). Squaring Equation 3.5

and bringing the constant term to the left hand side, one obtains the expression of the decomposition of variance, in the following form:

$$\int \mathcal{M}^2(\mathbf{x})d\mathbf{x} - \mathcal{M}_0^2 = \sum_{s=1}^{d} \sum_{i_1<..<i_s}^{d} \int \mathcal{M}_{i_1...i_s}^2 dx_{i_1}...dx_{i_s}, \tag{3.7}$$

that can be written as follows, given that the left hand side is the variance of $\mathcal{Y}$ and the right hand side is composed of variance terms:

$$\sigma_{\mathcal{Y}}^2 = \sum_{i=1}^{d} V_i + \sum_{i_1<...<i_s}^{d} V_{ij} + ... + V_{12...d}, \tag{3.8}$$

where:

$$V_i = Var(M_i(x_i)) \tag{3.9}$$

$$V_{ij} = Var(M_{ij}(x_i, x_j)) \tag{3.10}$$

Indices are typically normalised by the value of $\sigma_{\mathcal{Y}}^2$, leading to the expression:

$$\tilde{\sigma}^2(\mathcal{Y}) = \sum_{i=1}^{d} \mathcal{S}_i + \sum_{1\leqq i<j\leqq d} \mathcal{S}_{ij} + \sum_{1\leqq i<j<l\leqq d} \mathcal{S}_{ijl} \ + \ ... \ + \ \mathcal{S}_{12..d}, \tag{3.11}$$

$\mathcal{S}_i$ are first-order indices of variable i, $\mathcal{S}_{ij}$ are second-order indices for the variables ij, and so forth.

The individual contributions to the variance of the output are normalised by the global variance of the output itself.

Whenever the contributions of interactions between two or more input variables to the output variance is not negligible, the summation of first-order indices is lower than one:

$$\sum_{i=1}^{d} S_i \leq 1. \tag{3.12}$$

In general it is expected that the summation over all the indices,

$$\sum_{i=1}^{d} \mathcal{S}_i + \sum_{1\leqq i<j\leqq d} \mathcal{S}_{ij} + \sum_{1\leqq i<j<l\leqq d} \mathcal{S}_{ijl} \ + \ ... \ + \ \mathcal{S}_{12..d} \geq 1, \tag{3.13}$$

will be higher than one. This happens because of overlapping contributions of interaction terms. In fact there is normally overlap between the terms $\mathcal{S}_{ij}$, $\mathcal{S}_i$, $\mathcal{S}_j$.

This technique is particularly useful when wanting to understand which input variables

has the most impact in describing the variability of the output.

3.3. Surrogate Modeling

Forward propagation of the uncertainties and the sensitivity analysis typically require a large number of evaluation of the function one is interested in. The model considered in this work is a CFD solver, that although less expensive than a high-fidelity one, still requires some minutes to converge to a solution. The computational time that would be needed to perform a sensitivity analysis and the propagation of uncertainty would clearly be extremely high. Surrogate models play an important role in reducing this computational time. Surrogate modelling is in fact a technique used to approximate complex and expensive models with cheaper and faster ones. Any simplified model that can be used instead of a more expensive one to obtain a faster and cheaper output can be considered a surrogate model. For this thesis, two surrogate models have been considered. The Kriging one, extensively used also in hypersonic and UQ applications, and a Neural Network.

3.3.1. Kriging model

A Kriging model is a model based on a statistical interpolation resulting form the realisation of a Gaussian process that allows the interpolation of complex functions. A Kriging metamodel can be described by the following equation, as presented in [36].

$$\mathcal{M}^K(\mathbf{x}) = \beta^T \mathbf{f}(\mathbf{x}) + \sigma^2 Z(\mathbf{x}, \omega), \tag{3.14}$$

where the inputs (or training samples) of the model are collected in the experimental design $\mathcal{X} = \{\mathbf{x}^1, ..., \mathbf{x}^\mathbf{N}\}$; the corresponding responses are collected in $\mathcal{Y} = \{y^1 = \mathcal{M}(\mathbf{x}^1), ..., y^N = \mathcal{M}(\mathbf{x}^\mathbf{N})\}$. The first term in Equation 3.14 , $\beta^T \mathbf{f}(\mathbf{x})$ represents the trend (the mean value) of the Gaussian process; it consists of P functions f_j with $j = 1, ..., P$ with coefficients β_j. The second term is the multiplication between the variance of the Gaussian process (σ^2) and a zero-mean, unit-variance, stationary Gaussian-process $Z(\mathbf{x}, \omega)$. The probability space is defined in terms of a correlation function $R = R(\mathbf{x}; \mathbf{x}'; \theta)$ that represents the correlation between two sample points of the training (input) space. The vector ω represents weights associated to the different samples of the input, whereas θ is an hyperparameter influencing how much or how little samples are correlated. This hyperparameter can either be the same for all the dimensions of the input (isotropic correlation functions), or it can be a different value for each one of the dimensions of the input space. In this case one talks about anisotropic correlation functions. The Kriging

models used in this work are all based on the Matern correlation function [38]:

$$R_{matern}(x,x';\theta,\nu)=\frac{1}{2^{\nu-1}\Gamma(\nu)}\left(2\sqrt{\nu}\frac{|x-x'|}{\theta}\right)^{\nu}\mathcal{K}_{\nu}\left(2\sqrt{\nu}\frac{|x-x'|}{\theta}\right); \tag{3.15}$$

the parameter θ is the correlation function scale parameter, $\nu > 0.5$ is a parameter influencing the shape of the correlation function, $\mathcal{K}_{\nu}$ is the modified Bessel function and Γ is the Euler's Gamma function. The models built thrpoughout this essay are all constructed with $\nu = 5/2$. The associated function reads:

$$R(x,x';\theta,\nu=5/2)=\left(1+\sqrt{5}\frac{|x-x'|}{\theta}+\frac{5}{3}\left(\sqrt{5}\frac{|x-x'|}{\theta}\right)^{2}\right)\left[\frac{|x-x'|}{\theta}\right]. \tag{3.16}$$

The optimisation of the unknown parameters is performed through the Maximum-likelihood estimation. This technique find the set of Kriging parameters such that the likelihood function of the observations is maximised. Further details can be found [ref]. The optimisation problem is based on noise-free measurements.
Kriging models are powerful tools for providing predictions for a new point $\mathbf{x}$ outside of the experimental design $\mathcal{X}$. The prediction of the model, $\hat{Y} = \mathcal{M}^{K}(\mathbf{x})$, has a joint Gaussian distribution:

$$\begin{bmatrix}\hat{Y}(\mathbf{x})\\ \mathcal{Y}\end{bmatrix}\sim\mathbf{N}_{N+1}\left(\begin{bmatrix}\mathbf{f}^{T}(\mathbf{x})\beta\\ \mathbf{F}\beta\end{bmatrix},\sigma^{2}\begin{bmatrix}1 & \mathbf{r}^{T}(\mathbf{x})\\ \mathbf{r}(\mathbf{x}) & \mathbf{R}\end{bmatrix}\right), \tag{3.17}$$

where $\mathbf{F}$ is the observation matrix of the Kriging metamodel ($F_{ij} = f_j(\mathbf{x}^i)$, $i = 1, ..., N$; $j = 0, ..., P$), $\mathbf{r}(\mathbf{x})$ is the vector of cross-correlations between the prediction point $\mathbf{x}$ and the observations $\mathbf{x}^i$ ($r_i = R(\mathbf{x}, \mathbf{x}^i; \theta)$, $i = 1, .., N$ and $\mathbf{R}$ is the correlation matrix whose elements are $R_{ij} = R(\mathbf{x}^i, \mathbf{x}^j, \theta)$. Each prediction is a normal distribution.
The mean and variance of the prediction can be computed as follows:

$$\mu_{\hat{Y}}(\mathbf{x})=\mathbf{f}(\mathbf{x})^{T}\hat{\beta}+\mathbf{r}(\mathbf{x})^{T}R^{-1}\left(\mathcal{Y}-\mathbf{F}\hat{\beta}\right), \tag{3.18}$$

$$\sigma_{\hat{Y}}(\mathbf{x})=\sigma^{2}\left(1-\mathbf{r}^{T}(\mathbf{x})\mathbf{R}^{-1}\mathbf{r}(\mathbf{x})+\mathbf{u}^{T}(\mathbf{x})\left(\mathbf{F}^{T}\mathbf{R}^{-1}\mathbf{F}\right)^{-1}\mathbf{u}(\mathbf{x})\right), \tag{3.19}$$

where:

$$\hat{\beta}=\left(\mathbf{F}^{T}\mathbf{R}^{-1}\mathbf{F}\right)^{-1}\mathbf{F}^{T}\mathbf{R}^{-1}\mathcal{Y}\,,\quad \mathbf{u}(\mathbf{x})=\mathbf{F}^{T}\mathbf{R}^{-1}\mathbf{r}(\mathbf{x}-\mathbf{f}(\mathbf{x})). \tag{3.20}$$

The Kriging predictor is interpolative with respect to the points of the experimental design for which the variance $\sigma_{\hat{Y}}$ collapses to zero.

3.3.2. Artificial Neural Network

Artificial neural network (ANN) are a class of models used to make predictions based on an input data, also known as training set. The fundamental unit of such a network, is called neuron. Layers of neurons compose the structure of the network. Layers are interconnected and, thanks to activation functions associated to the different layers, weights and biases associated to the connections between neurons, it is possible to transform the input of the network to obtain the desired output.
A thorough description of the structures of ANN's is given in [12]; a brief description of the their key features is given below.
Let's consider a training set of N observations $LS = \{\mathbf{x}_1, ..., \mathbf{x}_N\}$, where all the observations are of dimensions n. It can be structured as follows:

0	$x_1(o)$	$x_2(o)$	...	$x_n(o)$	$y(o)$
1	x_1^1	x_1^2	...	x_n^1	y^1
2	x_2^1	x_2^2	...	x_n^2	y^2
⋮	⋮	⋮	⋮	⋮	⋮
N	x_1^N	x_2^N	...	x_n^N	y^N

Table 3.1: Ordering of a training set with the corresponding observations so as to make notation clearer.

The set of observed output is $y^i = y(\mathbf{x}^i)$. The most common ANN structure is the *multilayer perceptron* made of multiple layers of neurons fully connected to the next.
The total number of layers is called L, with layer 1 being the input layer, layer L being the output one and layers 2 to $L-1$ called hidden layers.
We can define the following set of relevant quantities:

- s_l $(1 \leq l \leq L)$ represents the number of neurons in the l-th layer
- $a_i^{(l)}(\mathbf{x})$ $(1 \leq l \leq L, (1 \leq i \leq s_l))$ is the output of the i-th neuron of layer l for an object $\mathbf{x}$
- f^l is the activation function of layer l
- $w_{i,j}^l (1 \leq i \leq s_{l+1}, 1 \leq j \leq s_l)$ being the weight of the edge form neuron j in layer l to neuron i
- $w_{i,0}^l$ $(1 \leq i \leq s_{l+1})$ is the bias / intercept of neuron i in layer $l+1$.

Predictions can be computed as follows:

$$\mathbf{a}_i^{(1)}(x) = \mathbf{a}_i(x), \quad \forall i : 1 \leq i \leq n \tag{3.21}$$

$$\mathbf{a}_i^{(l+1)}(x) = f^{(l+1)}\left(w_{i,0}^{(l)} + \sum_{j=1}^{s_l} w_{i,j}^{(l)} \mathbf{a}_j^{(l)}(x)\right), \quad \forall i, l : 1 \leq l \leq L, 1 \leq i \leq s_l \tag{3.22}$$

$$\tag{3.23}$$

that leads to the matrix form:

$$\mathbf{a}^{(1)}(x) = \mathbf{a}(x) \tag{3.24}$$

$$\mathbf{a}^{l+1}(x) = f^{l+1}\left(\mathbf{W}'^{(l)}\mathbf{a}'^{(l)}(x)\right) \quad \forall l : 1 \leq l \leq L. \tag{3.25}$$

The activation functions f^l play an important role in the structure of the network. Typical choices for this functions may include the sigmoid, hyperbolic tangent, ReLU and softplus functions. For a detailed discussion of the differences between the different activation functions one may address [32].

A reasonable, but not mandatory, selection of the activation functions may be that of using linear functions for the input and output layer of the network. Non-linear, but still differentiable activation functions can on the other hand be used for the hidden layers. A linear activation function at the input layer prevent the data from being distort before being processed by the network, while the same type of activation functions are useful at the output layer of the network because it allows for continuous real output values easier to interpret. Non-linear activation functions for the hidden layers are on the other hand generally preferred because they can more easily make the classes of the input space linearly separable by the output layer.

Defined the structure of the network and the activation functions to be used, the hyper-parameters of the the different functions and the weights are to be tuned.

This optimisation is achieved defining a loss function to be minimised. A loss function $\mathcal{L}$ compares the output layer predictions for an object $\mathbf{x}$ to the true outputs; calling $\mathcal{W}$ the set of parameters to be optimised, and the prediction of the network $\mathbf{g}(\mathbf{a}(\mathbf{x}); \mathcal{W})$, one wants to find the set of parameters $\mathcal{W}$ that minimises the average loss over the training data:

$$\mathcal{W}^* = arg\min_{\mathcal{W}} \frac{1}{N} \sum_{x \in LS} \mathcal{L}(\mathbf{g}(\mathbf{a}(\mathbf{x}); \mathcal{W}), \mathbf{y}(x))$$

Iterative optimisation techniques are used to find the optimal set of parameters $\mathcal{W}$. Many of these optimisation techniques are based on the computation of the gradient of the loss function with respect to the weights. For this reason, differentiable activation functions

are preferred.

3.4. Summary

An introduction to some Uncertainty Quantification (UQ) and Surrogate modelling techniques relevant for this work has been given in this chapter. Forward propagation techniques have been briefly presented, given their relevance in understanding how uncertainties in the inputs of a model result in uncertainties in the output of the model itself. Two different approaches for performing sensitivity analysis of models have been introduced before a brief revise of the mathematical modelling of two surrogate modelling techniques, the Kriging model and the artificial neural network in its simplest form, the multilayer perceptron.

4 | Analysis of Nitrogen-Graphite Interactions in VKI Plasmatron

The first three chapter have introduced the scope of this thesis and the experimental and numerical tools exploited to achieve it.
This chapter is divided into two sections: the first is dedicated to the analysis and elaboration of the data provided by two experimental campaigns conducted in the VKI Plasmatron facility aimed at understanding the interaction between nitrogen plasma flow and carbon-based thermal protection system.
The second part of the chapter is dedicated to the deterministic simulation of the first experimental campaign, conducted at 15 hPa.

4.1. Analysis and review of experimental data

The first experimental campaign conducted in the VKI Plasmastron for the testing of carbon-based ablation shields in nitrogen plasma flow is composed of four experiments at increasing Plasmatron power and constant chamber pressure of 15 hPa. The samples are machined in-house with an hemispherical shape of 25 mm radius and a cylindrical after-body of 25 mm.
Table 4.1 summarises the testing conditions for the four cases. The nomenclature of the different experiments follows the scheme: GX_Y_Z , where X indicates the type of graphite grain used, Y represents the chamber pressure in hPa and Z is the power in kW of the Plasmatron.
The letter X has value 1 when the first grain type is used, characterised by a density of 1760 kg/m^3, whereas it assumes value 8, when the second type of grain is used, whose density is 1810 kg/m^3 . The same nomenclature is used for the second testing campaign.
As described in Section 2.1.2, a digital camera has been used for obtaining the recession

rate and the wall temperature has been measured with a pyrometer.

ID	p_d	p_{el}	$\dot{q}_w$	τ_{ss}	T_w	$\dot{s}$	Δm
	Pa	kW	kW/m^2	s	K	µm/s	g
G1_15_280	231	280	2130	266	2225	1.41	2.00
G1_15_330	268	330	2730	250	2410	1.64	2.05
G1_15_370	312	370	3500	300	2535	2.60	2.4
G1_15_390	330	390	3580	277	2575	2.51	2.1

Table 4.1: Summary of the 15 hPa experimental campaign test conditions. Reported are the measured sample temperature, dynamic pressure and heat flux, the electrical power provided to the generator, the recession rate and the ablated mass.

The rebuilding technique briefly described in Section 2.1.3 has been used by Helber [14] to retrieve the temperature and the velocity at the edge of the boundary layer. The retrieved quantities and the experimentally measured mass flow rates with relative uncertainties are given in Table 4.2
. They are taken from the work of [14].

ID	ρ_{mat}	p_s	T_e	u_e	$\dot{m}$
	kg/m^3	hPa	K	m/s	g/m^2/s
G1_15_280	1760	15	10005	554	2.49 ± 0.91
G1_15_330	1760	15	10280	562	2.89 ± 0.97
G1_15_370	1760	15	11040	846	4.41 ± 0.80
G1_15_390	1760	15	10970	859	4.56 ± 0.70

Table 4.2: Summary of the rebuilt condition at the edge of the boundary layer for the 15 hPa campaign alongside the experimentally measured blowing mass rate and relative uncertainty.

There seems to be a proportionality between the wall temperature and the blowing mass flow rate with both growing as the power supplied to the generator of the Plasmatron increases.
Contrary to the first experimental campaign, both graphite grain types have been tested in the second campaign; the pressures tested are higher. Two experiments at 100 hPa and two experiments at 200 hPa have been run for both grain types. Data for the wall temperature, the recession thickness, the ablated mass and the dynamic pressure alongside

the testing condition in terms of pressure and power are reported from a technical report written at the von Karman Institute [22].

ID	p_s	p_d	p_{el}	T_w	Δs	Δm
	hPa	Pa	kW	K	mm	g
G1_100_370	100	56.7	370	2613	0.24	1.51
G1_100_400	100	66.9	400	2729	0.22	1.18
G1_200_370	200	36.2	370	2663	0.16	0.98
G1_200_400	200	42.5	400	2709	0.22	1.18
G8_100_370	100	58.8	370	2596	0.29	1.17
G8_100_400	100	70.2	400	2694	0.39	1.07
G8_200_370	200	33.4	370	2609	0.20	0.68
G8_200_400	200	39.3	400	2678	0.26	0.67

Table 4.3: Summary of the second experimental campaign test conditions. Reported are the measured sample temperature, dynamic and static pressure, recessed thickness and ablated mass.

The experimental data of the recorded temperature has been analysed so as to retrieve the steady state time and to quantify the uncertainties on the blowing mass rate.
As it is shown in Figure 4.1 the recorded temperature at the wall reaches steady state after around 60 seconds from the beginning of the experiment. A function of the form:

$$Y = ae^{bx} + ce^{dx} \tag{4.1}$$

has been fitted on the raw data so as to filter them. The optimisation process is solved minimising the least squares error between the model and the data using a Levenberg-Marquadt algorithm [24], optimised for this kind of non-linear least squares analysis where a number n_{obs} is used to fit a n_{param} model with n_{obs} being significantly bigger than n_{param}. Figure 4.1, reported below, shows the experimental record of the sample temperature in blue and the fitted function in dotted red line. Similar images for all the eight experimental tests are given in Appendix A.

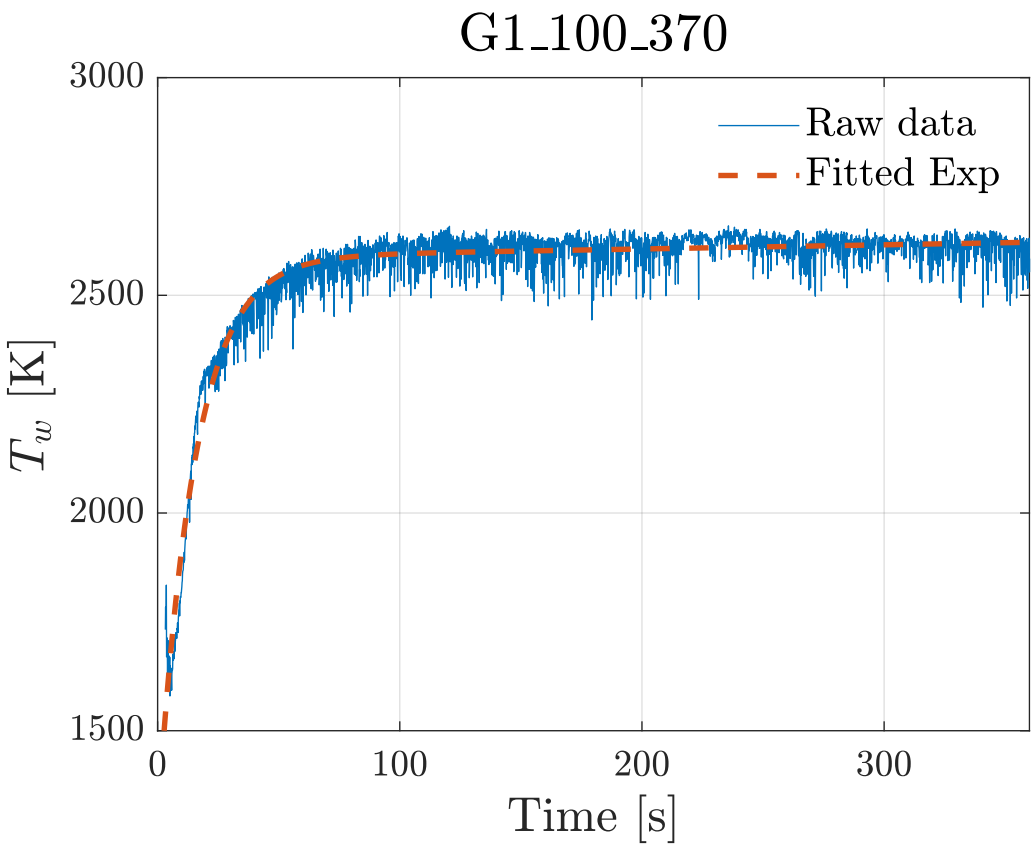

Figure 4.1: Record of the sample temperature during the execution of the first experiment of the second experimental campaign. Above experimental data, a fitted exponential-like function in the least squares sense is reported as a dotted red line.

The maximum temperature reached by the fitted model is identified. The uncertainty range of the starting point of the steady state ablation time is then identified ; the upper value is the time where the sample temperature reaches the 97% of the maximum value, whereas the lower bound is identified as the time when the temperature reaches 2000 K. Over this temperature, reactions causing ablation of the sample are fully activated. The point-like value of the steady state time is considered to be the mean between the minimum and maximum value of the uncertainty range. The experiment ends after 360 seconds. The value of the temperature reported in Table 4.4 is the mean temperature of the sample from the moment the sample reaches 97% of the maximum temperature and the end of the experiment.
The blowing mass flow rate is obtained as follows:

$$\dot{m} = \frac{\Delta s}{\tau_{ss}} \rho_{mat} \tag{4.2}$$

No uncertainty on the densities of the samples has been considered, whereas as reported by Helber [14], the ablated thickness is known with a standard deviation of 0.03 mm. Measurements are considered to be distributed as a Gaussian. The uncertainty range on the steady state time, obtained as explained above, is considered to be a 95% confidence interval. The propagation of the error (twice the standard deviation value) through the formula 4.2 writes:

$$\frac{err_{\dot{m}_i}}{\dot{m}_i} = \sqrt{\left(\frac{err_{\Delta s_i}}{\Delta s_i}\right)^2 + \left(\frac{err_{\tau_i}}{\tau_i}\right)^2 + \left(\frac{err_{\rho_i}}{\rho_i}\right)^2}, \tag{4.3}$$

with the error on the density being zero.

ID	ρ_{mat}	τ_{ss}	$T_{w,ss}$	$\dot{m}$	$\Delta\dot{m}$
	kg/m^3	s	K	g/m^2/s	g/m^2/s
G1_100_370	1760	300.99	2604	1.403	0.414
G1_100_400	1760	315.86	2725	1.226	0.361
G1_200_370	1760	305.95	2660	0.920	0.369
G1_200_400	1760	309.55	2704	1.592	0.399
G8_100_370	1810	290.63	2575	1.806	0.508
G8_100_400	1810	300.99	2688	2.345	0.515
G8_200_370	1810	280.27	2601	1.292	0.486
G8_200_400	1810	301.44	2674	1.561	0.434

Table 4.4: Summary of the analyses performed on the experimental data of the second campaign. Reported are the steady state time, the sample temperature, the blowing mass rate and its relative uncertainty (± 2 standard deviations).

The main goal of the analyses described in the previous Section has been the retrieval of the experimental blowing mass flow rates for the different tests with their relative uncertainties. The range obtained is to be compared with numerical simulations performed with the simulation tools described in Chapter 2.4.
The results of the simulations are given in the following Section.

4.2. Deterministic simulation of a low pressure experimental campaign

Obtained the values of the experimental blowing mass rate and their relative uncertainties it is possible to understand how the simulations performed with the Prata model and with the Capriati version compare with respect to the experimental results.
First, the simulation of the low pressure campaign tests is considered. As described in Chapter 2.4 the Stagline 1D solver is coupled with Mutation++ for obtaining the thermodynamics and transport properties and for solving the mass surface balance.
The rebuilding procedure described in Section 2.1.3 allows one to obtain the boundary conditions in terms of boundary layer edge temperature and edge velocities (values reported in Table 4.2); other boundary conditions are the pressure (15 hPa for all the four cases) and the sample wall temperature (reported in Table 4.1).
The gas surface interactions are described by the set of reactions reported in Table 2.1 with values of the rate coefficients shown in Table 2.2.
Starting from the outer radius of the sample, located at 25 mm from the origin of the domain, the line over which the simulation is performed extends up to 15.096 cm from the origin.
A convergence study on the number of grid points to be used is displayed in Figure 4.2 and Figure 4.3. The convergence on the simulated blowing mass rate for two test cases, one at 100 hPa and one at 200 hPa is shown.
A uniformly spaced grid is considered. In the case of the simulation at 100 hPa, it emerges that after 1000 points the output of the simulations remains constant, whereas 1200 points are needed in the case of the simulation at 200 hPa. Given this analysis, it has been decided to use 1000 points for the deterministic simulations of the test cases whose chamber pressure is 100 hPa and 1200 points for the ones characterised by a chamber pressure of 200

hPa.

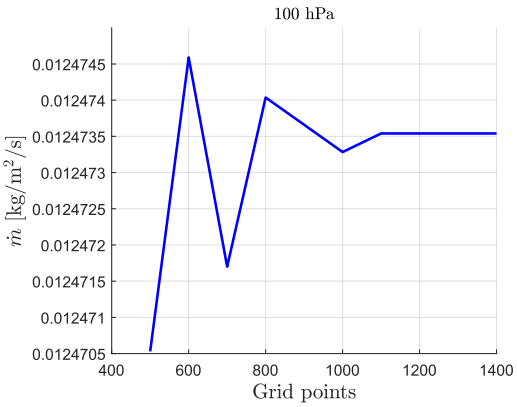

Figure 4.2: Grid convergence study for the G1_100_400 test case.

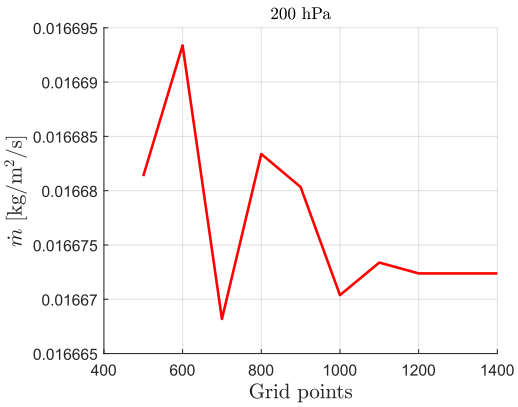

Figure 4.3: Grid convergence study for the G1_200_400 test case.

A schematic of the numerical simulation is given in Figure 4.4.

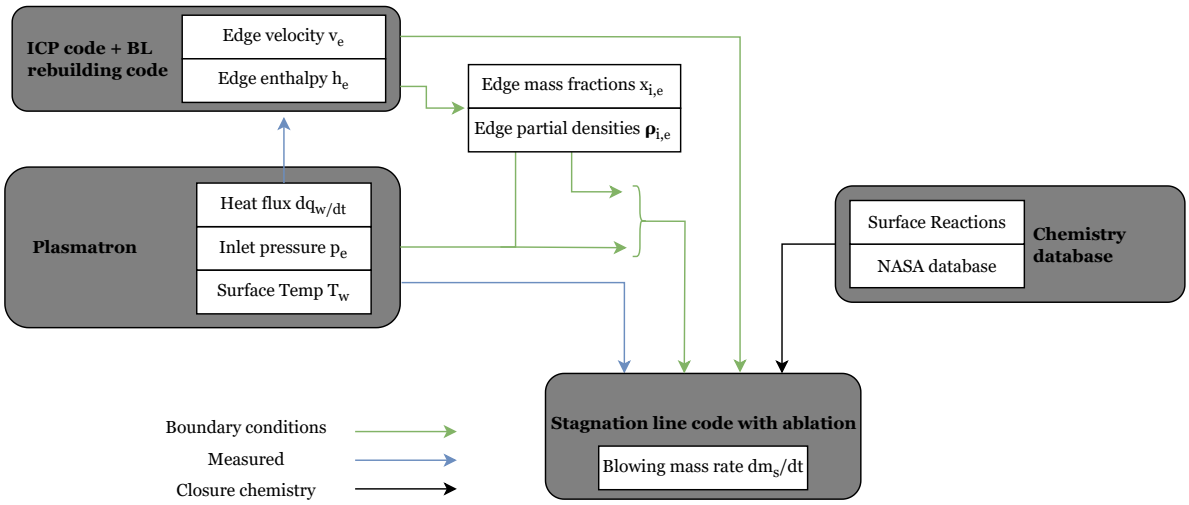

Figure 4.4: Scheme of the relations between the different codes used to perform the deterministic simulations of the first campaign.

Two deterministic simulations are thus run for each of the four experiments, one with the rate coefficients proposed by Capriati, one with the rate coefficients proposed by Prata. A comparison between the numerical results and the uncertainties on the experimental results is shown in Figure 4.5.

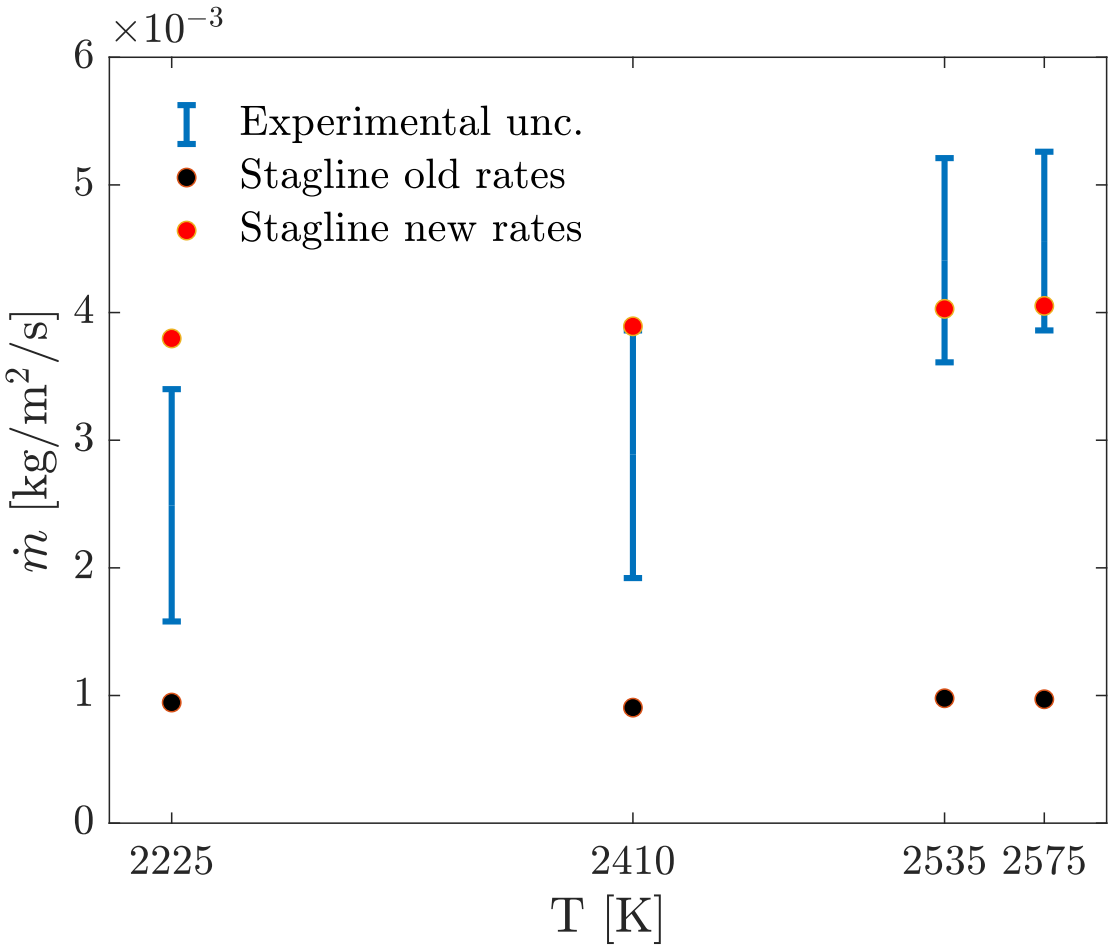

Figure 4.5: Comparison between the uncertainties on the experimental results and the numerical results obtained with Stagline solver. Black dotes are the results obtained with the rates of Prata, red dots are the ones obtained with the Capriati ablation model.

One can see that the model proposed by Capriati seems to better follow the proportionality between the temperature of the sample and blowing mass rate showed by the experimental results. Simulations with the Prata model appear to be almost insensitive to the sample temperature. Three of the four numerical results obtained with the Capriati version of the ablation model fall in the experimental uncertainty range, whereas none of the simulations with Prata's ablation model falls in the uncertainty ranges.
Similar results have been obtained by Capriati [6].

This proves that the modifications to the rate coefficients proposed by Capriati improve the prediction of the model at pressure of 15 hPa.

4.3. Summary

This chapter reviewed the experimental data of the two experimental campaigns performed in the VKI Plasmatron before presenting the numerical simulations of the first low pressure campaign.
Simulations performed with the model proposed by Capriati return values of the quantity of interest, the total mass production rate at the stagnation point, closer to the one obtained experimentally with respect tp the simulations with the rates proposed by Prata.
Both the experimental campaign and the simulations with the Capriati model suggest an increase in the total mass production rate with increasing wall temperatures. This behaviour is not "seen" by the original Prata model.
These deterministic simulations neglected both experimental and the modelling uncertainties.
Simulations of the second campaigns cannot be performed deterministically given that the rebuilding technique used to retrieve the edge temperature couldn't be applied. For this reason, simulations that consider uncertainties on the experimentally measured quantities and on the edge temperature have to be considered. This is the main topic of the first part of the following Chapter.

5 | Analysis of model and experimental uncertainties on Nitrogen-Graphite interactions in VKI Plasmatron

In Chapter 4 the results of deterministic simulations of the low pressure campaign have been presented. Experimental data for the heat flux could not be collected during the second campaign, resulting in a loss of information on the boundary layer edge temperatures. For this reason deterministic simulations of the second campaign could not be performed. In this chapter Uncertainty Quantification techniques are first used to investigate the propagation of the experimental uncertainties on the numerical simulations with the Capriati's and Prata's versions of the ablation model. The lack of knowledge of the edge temperature is taken into account. The second part of the chapter is dedicated to the propagation of the model uncertainties of the version of the model proposed by Capriati.

5.1. Propagation of experimental uncertainties

Ideally, the propagation of the experimental uncertainties using numerical simulation tools would result in a distribution of the simulation outputs that is comparable with the distribution describing the uncertainty on the experimentally retrieved blowing mass rate. Seeing the uncertain experimental quantities as inputs of the numerical model, forward propagation techniques described in Section 3.1 can be used to obtain the uncertainty on the output of the numerical model one is interested in that, in the case of this work, is the blowing mass rate.
The measured quantities are known with some uncertainties given that they are measured with instruments:

- Chamber pressure (p_e) is known with a 1.5% standard deviation error

- Dynamic pressure (p_d) is measured with 1% standard deviation error
- Sample wall temperature (T_w) is known with a 0.5% standard deviation error

The lack of knowledge of the heat flux for the experiments of the second campaign prevents one from using the ICP code and the BL rebuilding code. The boundary layer edge temperature is thus unknown. For this reason, it seems appropriate to consider a really wide range around the value that this quantity is expected to assume and to consider a uniform distribution for describing the uncertainty on this parameter. Considering that the rebuilt edge temperature for tests in the Plasmatron with generator power of around 400 kW typically reaches values between 10000 K and 11000 K, it has been considered reasonable to take a uniform distribution in the range 9000K-12000K to describe the uncertainty on the edge temperature.
The edge velocity is obtained directly from the measured dynamic pressure as:

$$v_e = \sqrt{\frac{2p_d}{H\rho_{mix}}} \tag{5.1}$$

where ρ_{mix} is the density of the gas mixture at p_e, T_e and H is a correction factor used to take into account the discrepancy between the free stream velocity and the velocity at the edge of the boundary layer. It is considered to be equal to 1.14. The scheme of the numerical simulation, similar to the one used for deterministic simulations is shown below.

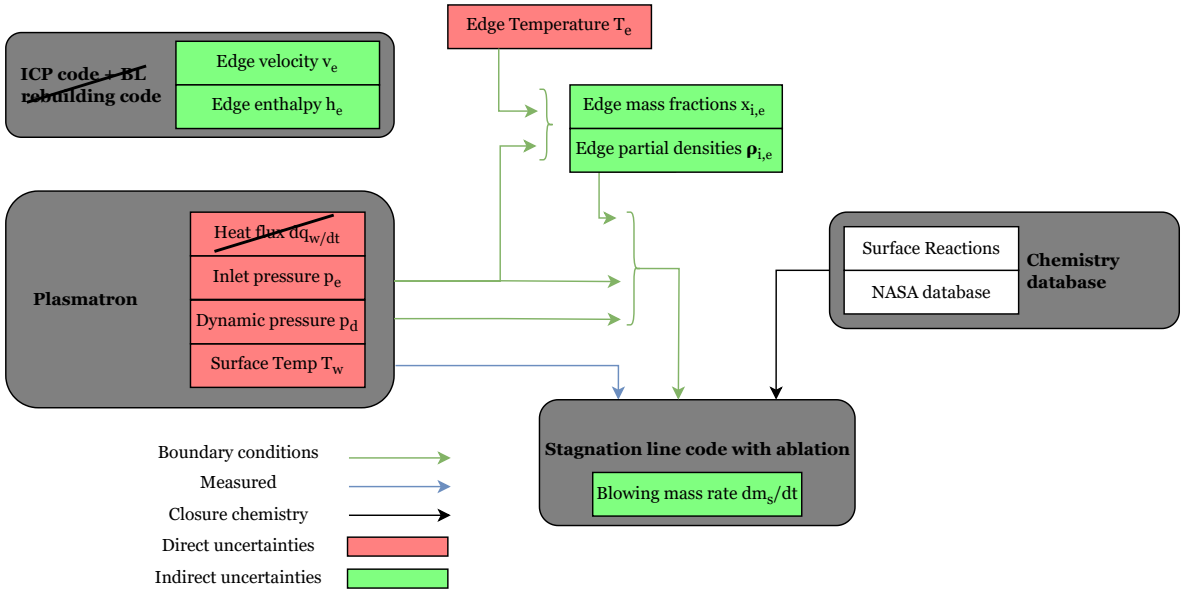

Figure 5.1: Scheme of the numerical simulations for the propagation of experimental uncertainties.

The vector of uncertain parameters is: $[T_w,\ p_d,\ T_e,\ p_e]$.
LHS sampling technique, described in Section 3.1, is used to efficiently propagate the uncertainties from the 4 parameter input space of the uncertain parameters. The edge temperature is considered uniformly distributed in the range 8000 K-12000 K for all the test cases of the second campaign, while the other three parameters are considered to be normally distributed around the nominal value of the parameter for the different test cases as reported in Table 4.3 .
One of the 8 cases has been analysed with a propagation of the different samples directly using the full numerical solver to compute the solution. The result of the propagation, comparing the results obtained with the Capriati model, the ones obtained with the Prata model and the experimental uncertainty on the measured mass flow are reported in Figure 5.11. 800 LHS samples sampled from the 4-parameter input space have been used to obtain the probability distributions of the Capriati and Prata models. Looking at Figure 5.11 one can see that for the case analysed, a test at 100 hPa, the propagation of

the experimental uncertainties using the model proposed by Prata intercepts part of the PDF representing the experimental results built as a Gaussian according to Table 4.4 (the error $\Delta\dot{m}$ being twice the value of the standard deviation). Simulations with the model proposed by Capriati overestimate the blowing mass rate. Moreover, looking at the two distributions obtained using Stagline coupled with Mutation++, it is evident that the one obtained with the model proposed by Prata is narrower than the one obtained with the model proposed by Capriati.

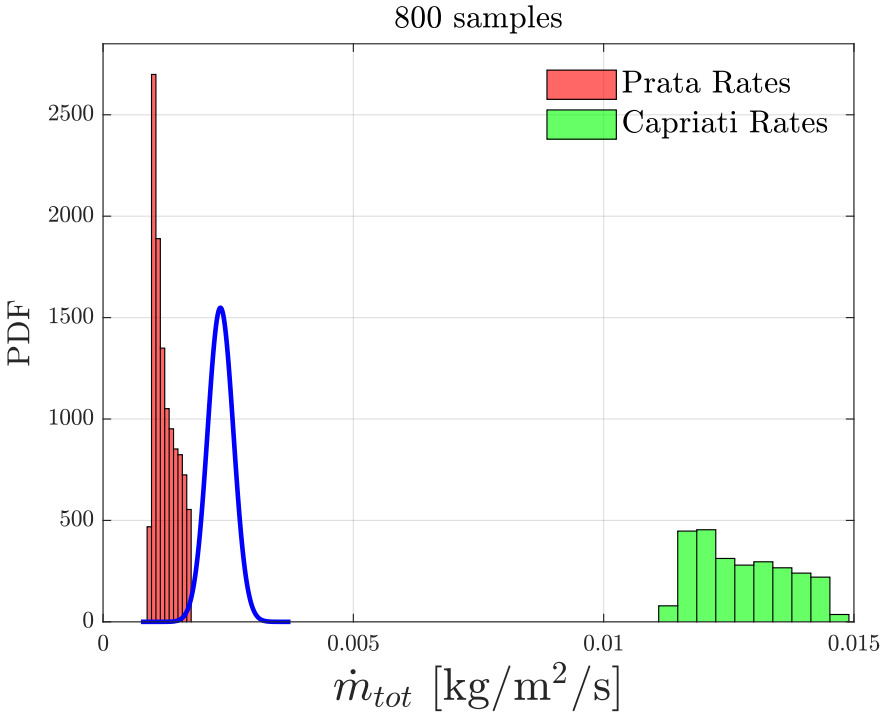

Figure 5.2: PDF distributions obtained from the propagation of experimental uncertainties using 800 LHS sample for the G8_100_400 test case.

The propagation of the LHS samples using the full numerical solver requires a considerable amount of time given that even though Stagline is a medium fidelity solver, some minutes are still required to get a converged solution for each simulation. For this reason, the propagation of thousands of samples, needed to obtain a converged PDFs for all the eight test cases, is really time consuming.
Surrogate models allows for a significantly faster propagation of samples, reducing the computational time needed to propagate all the samples.
In this work two type of surrogate models have been considered: Kriging models and artificial neural networks.
Training points have been obtained performing LHS sampling on a 4-parameter input

space with ranges for each variables covering all the eight experiment of the second testing campaign. More in particular, the 4 input parameters are considered uniformly distributed according to Table 5.1:

Variable	Distribution	Range
T_e	Uniform	8000 K - 12000 K
p_e	Uniform	90 hPa - 210 hPa
p_d	Uniform	35 Pa - 75 Pa
T_w	Uniform	2350 K - 2750 K

Table 5.1: Distributions of the parameters from which the LHS training points have been drawn.

It has been chosen to cover all the test cases with a single training set, so as to train a single surrogate model able to propagate experimental uncertainties for all the experimental test cases, rather than training a specific surrogate model for each one of the experimental cases. Doing so, the model built on the distributions covering all experimental conditions could be used to simulate new testing campaigns in the same range.
Kriging models and artificial neural networks have been preferred over other surrogate models techniques for multiple reasons.
The use of Kriging models is rather established in the context of Uncertainty Quantification analyses [16], [20]. Kriging models approximate well non-linear functions as long as the number of input dimensions/variables is rather low. A poorer performance is expected when approximating high-dimensional models. For this reason, it has been decided to compare the performance of Kriging models with a machine learning model. ANNs have been preferred over other machine learning models given their ability to handle well high-dimensional spaces with the space of uncertain parameters for the simultaneous propagation of model and experimental uncertainties being a 14-parameter model overall. Moreover, it was known that a rather large number of training points could be obtained, given the fact that a medium-fidelity solver was used. ANNs perform typically really well when a sufficiently large data set is available.
Kriging models have been trained using UQlab [23], a Matlab-based Uncertainty Quantification framework developed at the Chair of Risk, Safety and Uncertainty Quantification of ETH Zürich under the supervision of Prof. B. Sudret and Dr. S. Marelli.
The performance of the surrogate models has been estimated computing the root mean square mean error between the predictions of the models and the numerical solutions obtained with the Stagline solver coupled with Mutation++ on an independent test set of 150 test samples drawn in the training ranges with the LHS technique as well.

Data are normalised before training the neural network, avoiding problems coming from the fact that different order of magnitude characterise the different input variables. Data are normalised using means and variances of the training set according to:

$$s_i' = \frac{s_i - \mu_i}{\sigma_i}, \tag{5.2}$$

where i indicates one of the input variables and μ_i, σ_i are the mean and variance of variable i for the training set. Symbol s indicates both input training variables and output of the model (blowing mass rate).
Neural network is composed of two hidden layers, an input layer and an output layer.
As explained in Section 3.3.2, two linear activation functions has been used for the input and output layers and non linear hyperbolic tangent activation functions have been used for the two hidden layers.
Such a structure has been chosen given that it is the simplest one that has allowed to reach a sufficiently low error on the test set according to the procedure described below.
The number of neurons in the hidden layers is optimised according to the minimisation of the cross-validation error. Considering up to 20 neurons per layer, the performance of each combination of number of neurons per layer is estimated as follows: the training set is randomly shuffled and divided into 10 sub-sets. A neural network built with the combination of neurons per layer to be tested is then trained using nine of the ten sub-sets obtained. The root mean square error is introduced as a measure for evaluating the expected performance of a model. It is defined as:

$$RMSE = \sqrt{\frac{1}{n_t}\sum_{i=1}^{n_t}(y_i - \hat{y}_i)^2}, \tag{5.3}$$

where n_t is the number of test point used, y_i is the solution associated to test point i obtained with the full numerical solver, and $\hat{y}_i$ is the prediction for the same point obtained as realisation of the numerical model tested.
As it has been shown above, training and test points are normalised; for this reason the root mean square error defined in Equation 5.3 can be considered a normalised root mean square error (NMRSE).
This measure is calculated considering as test set the sub-set that has not been used for the training. The procedure is repeated until each of the ten sub-set is used as test set and the average of the root mean square error is used as error metric for evaluating the performance of the combination of neurons per layer. This error metric is called cross-validation error.

The combination minimising the cross-validation error is considered the optimal one.
Known the "optimal" structure of the net, an ensemble model is built; 50 neural networks built with the "optimal" structure are trained on the full training set using bootstrap sampling.
Bootstrap sampling is performed randomly drawing samples from an original dataset with replacement. Sampling a total number of samples equal to the number of training points from which samples are taken, it is statistically expected that around 30% of the sample are not included in each "bootstrap sampled set". The procedure is repeated until 50 networks are trained. The prediction of the ensemble model for a new sample is the mean of the predictions of the 50 models built. Building an ensemble model is preferable given that it generally improves accuracy and reduces over-fitting and variance. Predictions account for the normalisation process described above.
The performance of the ensemble model is finally estimated computing the root mean square error between the prediction of the ensemble model and the realisation of Stagline coupled with Mutation++ on a training set of 150 test samples, as it has been the case for the Kriging model.
The convergence of the error on the normalised root mean square error on the test set for the "optimised" neural network and the Kriging model is reported in Figure 5.3 and Figure 5.4 .
The "optimised" number of neurons per layer is 13, 12.

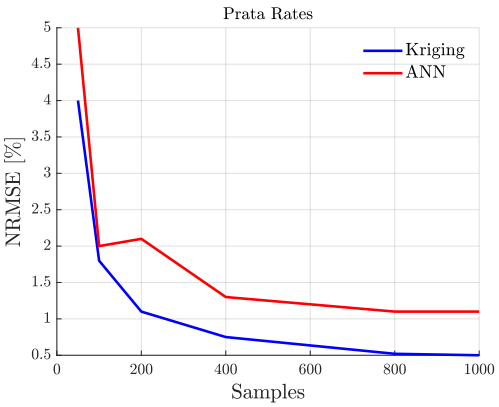

Figure 5.3: Convergence of the normalised root mean square error (NRMSE) between models predictions and full numerical solution for a test set of 150 samples. The numerical solutions obtained with the "optimised" ANN model and the Kriging model are compared with full numerical solutions obtained using Prata ablation model.

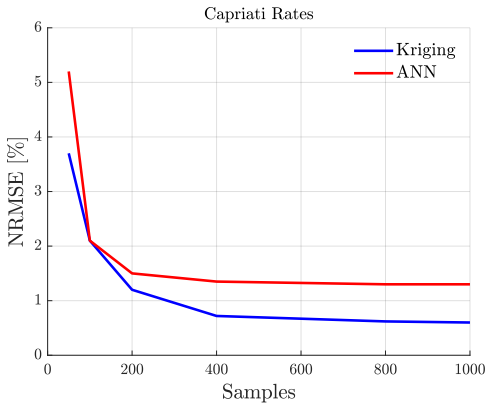

Figure 5.4: Convergence of the normalised root mean square error (NRMSE) between models predictions and full numerical solution for a test set of 150 samples. The numerical solutions obtained with the "optimised" ANN model and the Kriging model are compared with full numerical solutions obtained using Capriati ablation model.

As one can see the error computed using both the neural network and the Kriging model can be considered satisfactory (<2%) once more than 200 samples are used to build the training set. Doing so, the error on the training set, expected to be representative of the error on a general new prediction with respect to the full numerical solution, is lower than 2% for the ANN and lower than 1% for the Kriging model.
Overall, two Artificial Neural Networks and two Kriging Models have been trained, accounting for the two versions of the ablation model.
Alongside the quantitative measure of the root mean square error on the independent training set, a qualitative assessment of the validity of the surrogate models has been conducted.
Stagline coupled with Mutation++ has been used to solve independent samples on an input space representing the experimental uncertainties of two experimental tests of the second campaign: G1_200_370 and G8_100_400. This population lies in a 4 dimension space:

1. T_e: uniform distribution ranging from 8000 K to 12000 K;
2. p_e: normal distribution centered at 200 hPa for G1 test case and at 100 hPa for G8

test case with 1.5% standard deviation;

3. p_d: normal distribution centered at nominal value of the experiment (see Table 4.3) with 1% standard deviation;

4. T_w: normal distribution centered at nominal value of the experiment (see Table 4.3) with 0.5% standard deviation.

For each of the two cases, 800 samples have been drawn.
The predictions of the two surrogate models for these same samples and the full numerical solutions have been used to build the *qqplots* shown in Figure 5.5 and Figure 5.6 .

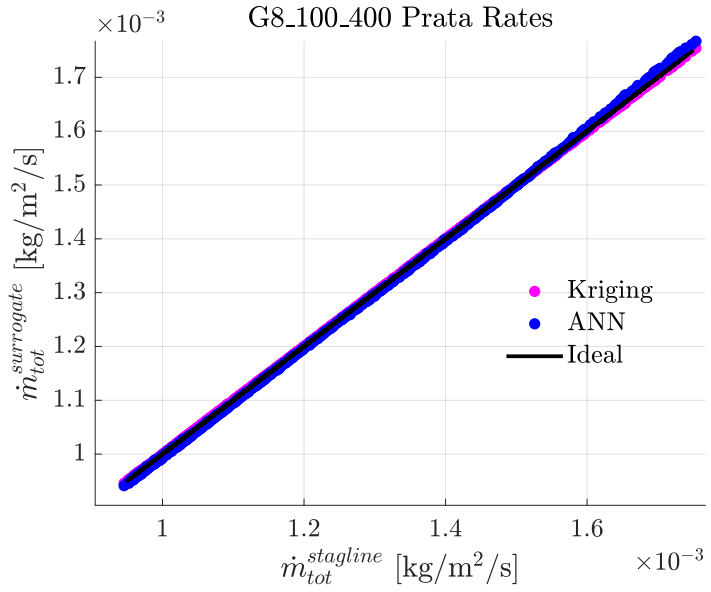

Figure 5.5: *Qqplot* for the G8_100_400 test case. Comparison between the full numerical solutions obtained with Prata's version of the ablation model and the predictions of the surrogate models for 800 samples drawn from a population describing the experimental uncertainties of the test case considered.

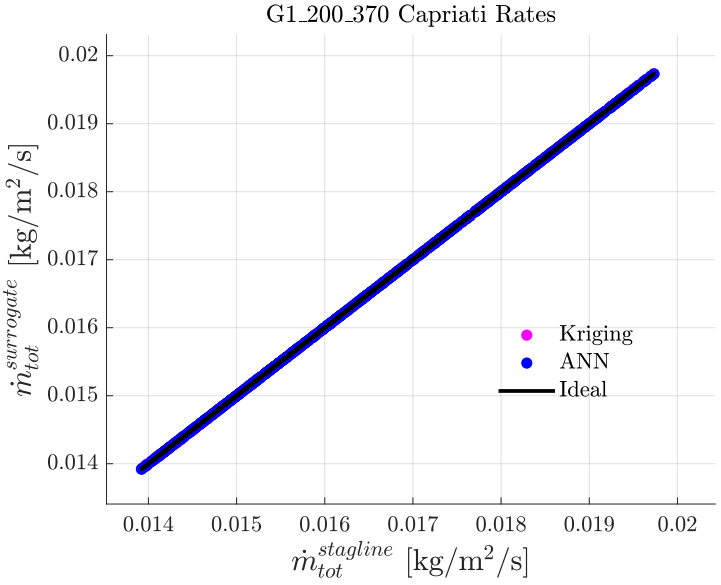

Figure 5.6: *Qqplot* for the G1_200_370 test case. Comparison between the full numerical solutions obtained with Capriati's version of the ablation model and the predictions of the surrogate models for 800 samples drawn from a population describing the experimental uncertainties of the test case considered.

The probability distribution functions obtained with the full numerical solution of the 800 samples drawn for each of the two experiments have been compared with the probability distribution functions obtained using the predictions of the two surrogate models for 5000 samples drawn from the same population the 800 samples have been drawn from.
The comparison is shown in Figure 5.7 and Figure **??**.
One can see that the distribution obtained with the surrogate models is an almost converged version of the same distribution obtained with the solution of the 800 samples obtained with the full numerical solver.
The converged distributions obtained with the Kriging model and with the ANNs are almost identical, with the exception of some minor differences in the right tail of the Prata rates.

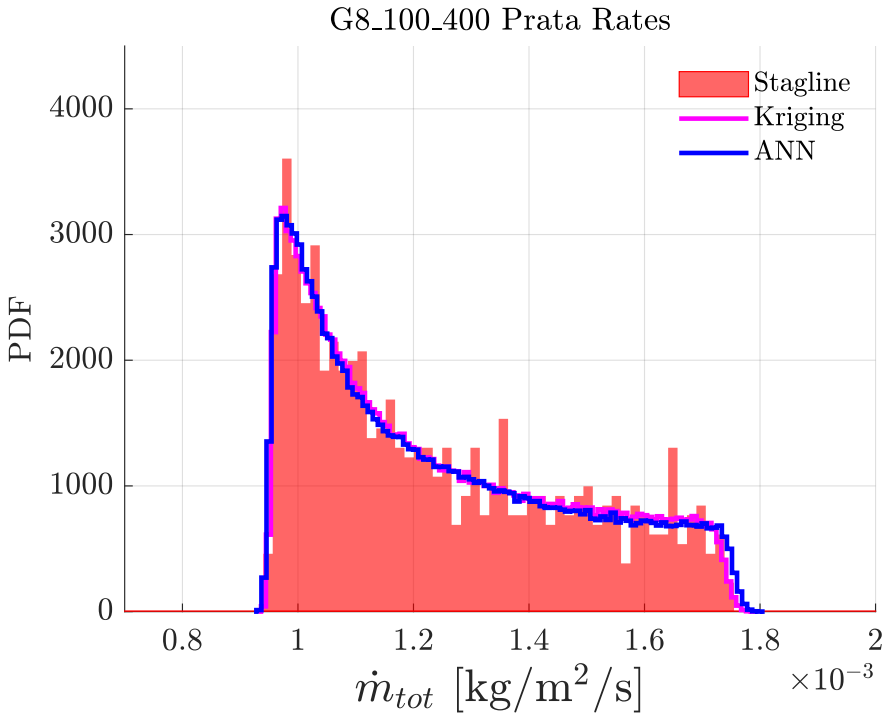

Figure 5.7: Comparison between the PDF obtained with 800 full numerical solutions and the propagation of 5000 samples using the Kriging and ANN surrogate models. Samples are drawn from a population describing the experimental uncertainties of the test case G8_100_400. Prata's ablation model is used.

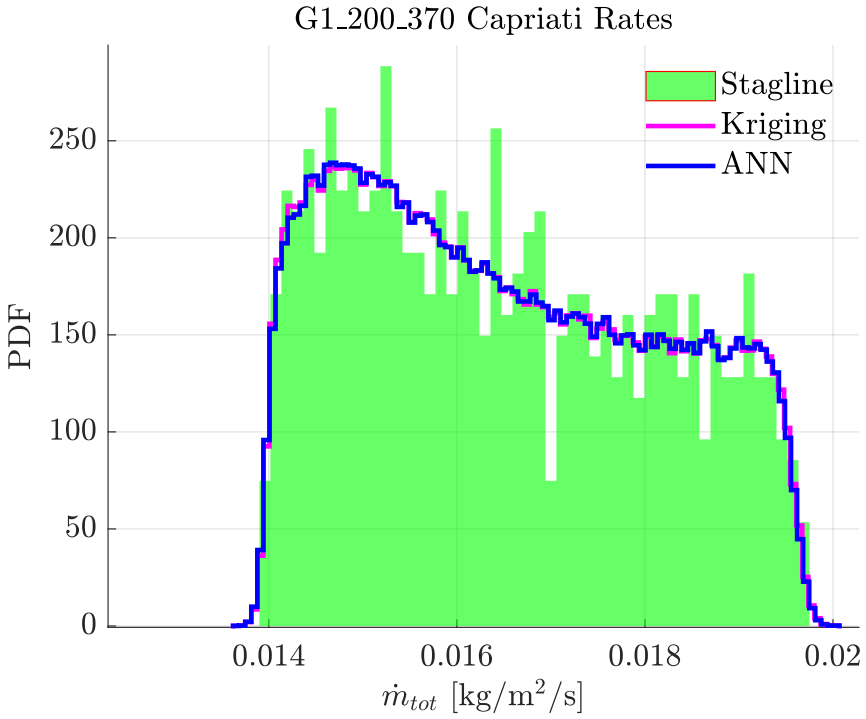

Figure 5.8: Comparison between the PDF obtained with 800 full numerical solutions and the propagation of 5000 samples using the Kriging and ANN surrogate models. Samples are drawn from a population describing the experimental uncertainties of the test case G1_200_370. Capriati's ablation model is used.

Having assessed the validity of the surrogate models in replacing the full numerical solver with quantitative and qualitative evaluations, it is possible to conclude that both the models can be used to enhance the speed of propagation of experimental uncertainties with little to no loss in the accuracy of the realisations.
Given the low-dimensionality of the problem, the Kriging model still performs really well and considering the complexity of the training of the neural network, one may probably prefer the Kriging model as surrogate model for the evaluation of the effect of experimental uncertainties on the blowing mass rate of the second campaign.
Considering the surrogate models valid substitutes of the full numerical solutions, it is possible to propagate the experimental uncertainties for all the eight test cases of the second campaign. In a similar fashion to what has been done for the drawing of the samples for the G1_200_370 and G8_100_400 test cases above, 5000 samples for each experimental test are drawn and the surrogate models are used to approximate the solutions.
Figure 5.9 and Figure 5.10 shows the propagation of the experimental uncertainties for all eight test cases using Kriging models and artificial neural networks. Bars represent the interpercentile range of the associated distribution.

Insights suggested by the analysis on the single experiment G8_100_400 performed with the full numerical solver are confirmed by the propagation made with surrogate models. Interpercentile ranges of the distributions obtained using surrogate models trained with the training points obtained using Prata's ablation model intercept partially the interpercentile ranges of the normal distributions built according to the experimental results and the uncertainties on the experimentally retrieved blowing mass rate. Results obtained with the surrogate models trained with points simulated using Capriati's model overestimate the blowing mass rate. The influence of pressure on Capriati's model is rather evident, whereas the model trained with Prata's ablation model seems to be more or less not influenced neither by the pressure nor by the temperature of the sample.

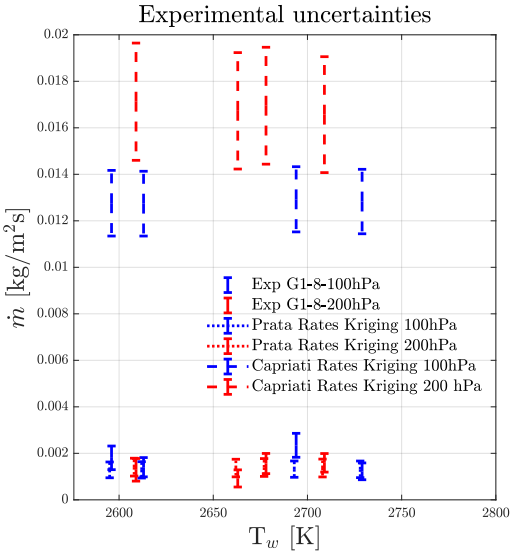

Figure 5.9: Comparison between the propagation of experimental uncertainties using Kriging models for both the Prata's and Capriati's versions of the ablation model. Solid line represents the uncertainties on experimental results. Interpercentile ranges are displayed for all the distributions. The analysis of the eight experimental tests of the second campaign is displayed.

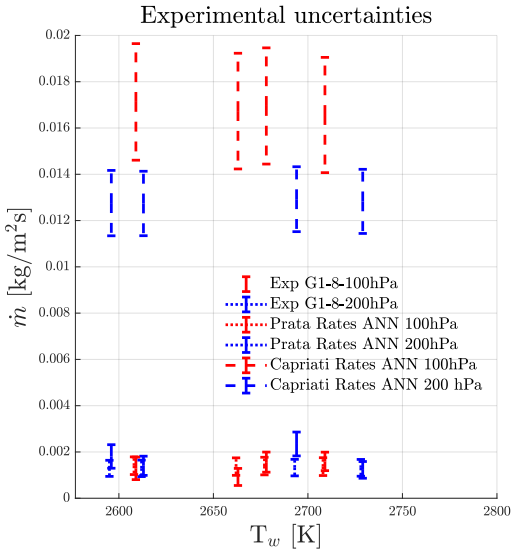

Figure 5.10: Comparison between the propagation of experimental uncertainties using artificial neural network models for both the Prata's and Capriati's versions of the ablation model. Solid line represents the uncertainties on experimental results. Interpercentile ranges are displayed for all the distributions. The analysis of the eight experimental tests of the second campaign is displayed.

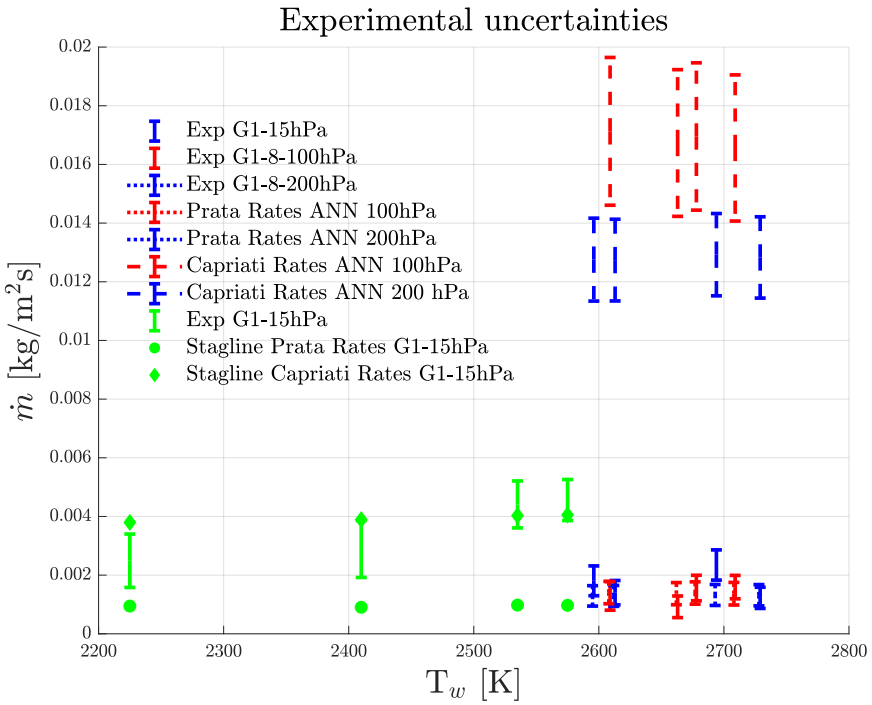

Figure 5.11: Comparison between the propagation of experimental uncertainties using artificial neural network models for both the Prata's and Capriati's versions of the ablation model. Dashed lines represent the uncertainties on experimental results. Interpercentile ranges are displayed for all the distributions. Experimental uncertainties and numerical simulations of the first campaign are also displayed.

The appropriateness of Capriati's ablation model in reproducing experimental tests at low pressure (15 hPa) has been shown in Chapter 4. Current section has on the other hand shown that Prata's version of the ablation model is more suitable for reproducing the results of the experimental campaign at higher pressures (100 hPa, 200 hPa). It is therefore interesting to look into how the input variables affect the outcome of the simulations using surrogate models at the scope of understanding where the discrepancies between the two models come from.
For this reason, the next section is dedicated to the sensitivity analysis of the two versions of the ablation model.

5.2. Sensitivity analysis of Prata and Capriati's Gas Surface Interaction models

The objective of a sensitivity analysis technique is establishing how much the variability of each input variable influences the variability of the output of the general model. As it has been described in Section 3.2, two types of sensitivity analysis has been conducted: a one-at-a-time analysis and the computation of the Sobol indices. Sobol indices have been computed using UQlab software exploiting Montecarlo propagation.
Results of the one-at-a-time analyses performed are displayed in Figures 5.12-5.19. One-at-a-time analyses has been performed for all the four uncertain input parameters ($[T_e, T_w, p_e, p_d]$). The analyses on the influence of the parameters on the blowing mass rate have been performed varying one input at a time in the ranges displayed in Table 5.1, except for the analysis of the influence of the edge pressure. A wider range has been used so as to understand when the difference between the predictions of the two models increases significantly.
Full numerical solutions for a limited amount of cases and 1000 samples using the Kriging and neural network surrogate models have been used to obtain Figures 5.12-5.19. The validity of the surrogate models in replacing the full numerical solution is once more confirmed. It is relevant to note that, considering the prediction of the surrogate models outside of the training ranges, the error with respect to the exact solution is significant; this is evident in Figure 5.16 .
The influence on the blowing mass flow rate varying one input parameter at a time is displayed in Figures 5.12, 5.13, 5.16, 5.17. Takeaways that can be drawn looking at the one-at-a-time sensitivity analyses on the blowing mass rate are the following:

- The model trained with Capriati's version of the ablation model is significantly more sensitive to edge pressure.
- Edge temperature and dynamic pressure seems slightly more influential in the Capriati's version.
- Influence of the variability of the wall temperature on the variability of the blowing mass rate is rather small for both models.

Given that the two versions of the ablation model differ for the values assigned to the rate-coefficients characterising the chemical reactions that describe the gas-surface interactions between the nitrogen plasma and the carbon ablative surface, it is interesting to perform one-at-a-time sensitivity analyses looking at the influence of the variability of the input parameters on the chemical production rates of each chemical species considered in the

model. Surrogate models have been trained for returning as output the blowing mass rate. For this reason, they cannot be used to perform an one-at-a-time analysis focusing on species chemical production rates. Instead, a limited number of numerical solutions obtained with Stagline coupled with Mutation++ have been used.
Looking at Figures 5.14, 5.15, 5.18, 5.19, a difference in the mechanisms favoured by the two models is noticeable. Prata's model favours recombination of nitrogen atoms into molecules, whereas the chemical path favoured by Capriati's model is the formation of CN molecules.

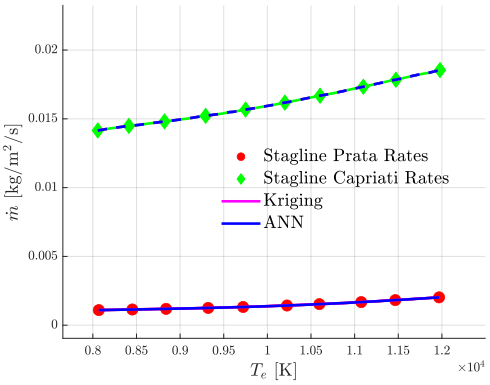

Figure 5.12: One-at-a-time sensitivity analysis. Edge temperature influence on blowing mass rate.

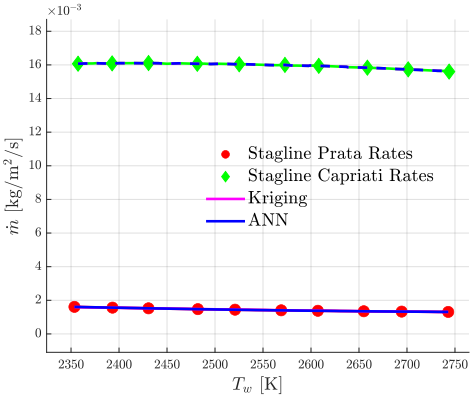

Figure 5.13: One-at-a-time sensitivity analysis. Wall temperature influence on blowing mass rate.

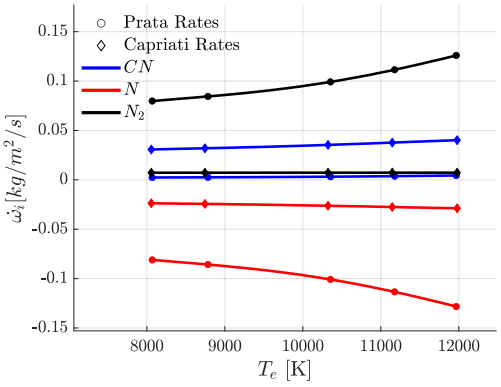

Figure 5.14: One-at-a-time sensitivity analysis. Edge temperature influence on chemical production rates.

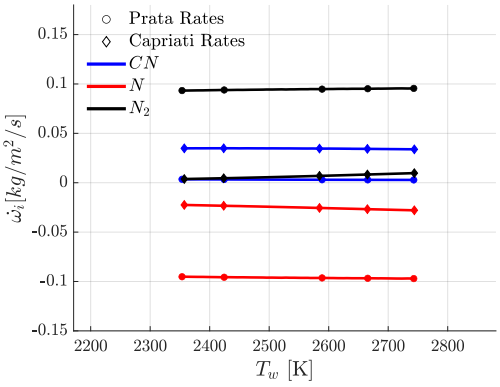

Figure 5.15: One-at-a-time sensitivity analysis. Wall temperature influence on chemical production rates.

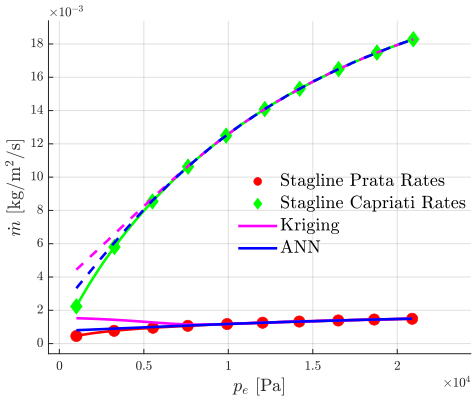

Figure 5.16: One-at-a-time sensitivity analysis. Chamber pressure influence on blowing mass rate.

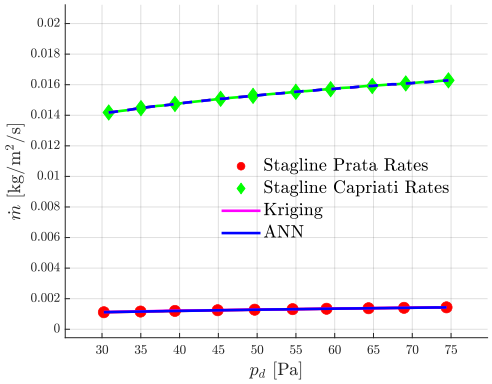

Figure 5.17: One-at-a-time sensitivity analysis. Dynamic pressure influence on blowing mass rate.

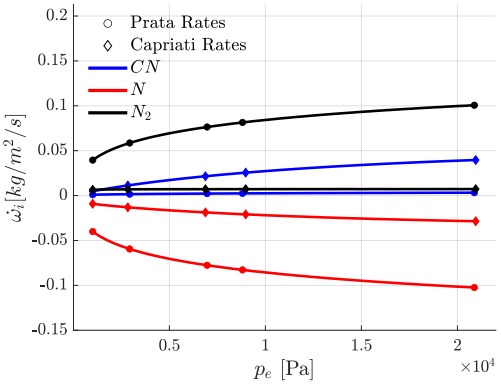

Figure 5.18: One-at-a-time sensitivity analysis. Chamber pressure influence on blowing mass rate.

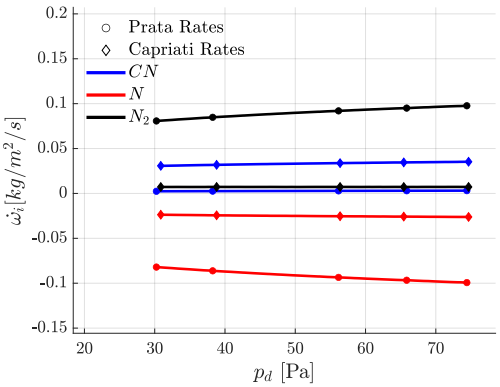

Figure 5.19: One-at-a-time sensitivity analysis. Dynamic pressure influence on chemical production rates.

First Order Sobol indices computed with Montecarlo propagation for the Neural Network Surrogate models are reported in Figure 5.20 and Figure 5.21.

Sobol indices are estimated through Montecarlo propagation generating a large number of samples for the input variables according to the distributions reported in Table 5.1. The components of the variance introduced from the variance decomposition explained in Section 3.2 are estimated from the model evaluations of the samples generated; additional sampling and averaging techniques are used to improve the accuracy of the estimation.

The variability of the blowing mass rate in the model trained with Prata's version of the ablation model is almost entirely described by the variability of the edge temperature, whereas the largest Sobol indices for the model trained with Capriati's version are the

ones associated to edge pressure and edge temperature. This results are in line with the one-at-a-time analysis performed.
Total Sobol indices are displayed; they coincide with first order ones given that second order indices are almost negligible.

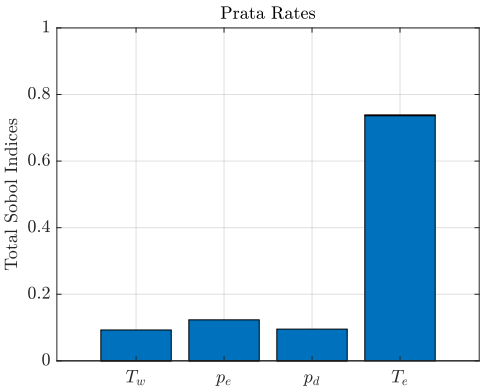

Figure 5.20: Total Sobol Indices of ANN surrogate model trained with Prata's version of the ablation model.

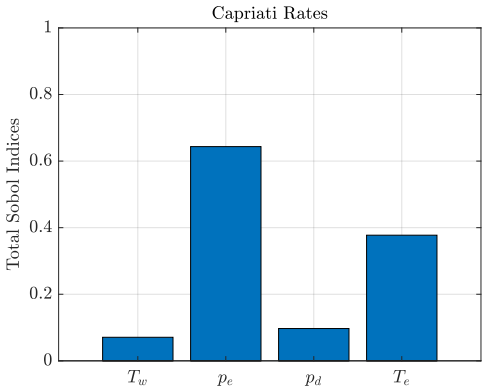

Figure 5.21: Total Sobol Indices of ANN surrogate model trained with Capriati's verison of the ablation model.

5.3. Propagation of model uncertainties

Thanks to the propagation of uncertainties on experimental inputs presented in Section 5.1 and thanks to the sensitivity analysis presented in the precedent Section 3.2, it has been possible to highlight some differences between the two versions of the ablation model and to understand which chemical pathways are favoured by each of the two.
The propagation of experimental uncertainties with Capriati's version overestimate the experimentally retrieved blowing mass rates for the higher pressure campaign. Prata's rates coefficients are deterministic, whereas Capriati's rates, as explained in Section 2.2.5, have been obtained in terms of probabilistic distributions. Given that the calibration of Capriati's rates has been performed using experimental results at low pressures (15 hPa), it is interesting to understand if propagating model uncertainties of this model, one can obtain interpercentile ranges for the second campaign that at least partially intercept the uncertainties of the experimentally retrieved blowing mass rate.
Wanting to do so, analyses similar to the ones presented in the previous Section (Section 5.1), has been conducted considering both experimental and model uncertainties.
The dimension of the vector of uncertain parameters grows from 4 (the experimental ones) to 14. Alongside the four experimental variables, the 10 model parameters calibrated with

a Markov Chain Monte Carlo method from Capriati [6] are considered. The uncertainties come directly from the distributoin of the rates themselves.
Following the nomenclature of Table 2.2, according to which rate coefficients for reaction r can be written in the form:

$$k_r = X_r exp\left(-\frac{E_r}{T_w}\right), \tag{5.4}$$

with symbol X_r represents a pre-exponential coefficient, and E_r being the activation energy and considering the ordering of the reactions used in the same table, the global vector of uncertainties reads: $([T_e, T_w, p_e, p_d, E_1, E_3, E_4, E_5, E_6, X_3, X_4, X_5, X_6, B])$.
With the objective of propagating samples from the distributions obtained by Capriati, a Kriging model and an artificial neural network have been trained using training points that would cover a 14-dimensional space defined in Table 5.2. This input space allows for the propagation of both model and experimental uncertainties given that the distributions for the rates obtained by Capriati are all contained in the ranges selected.
So as to ease the handling of some variables the logarithmic scale with base 10 is used $([X_3, X_4, X_5, X_6, B])$. Once again, it has been preferred to consider a wide range of input variables so as to train a single ANN model and a single Kriging model that can be used to propagate uncertainties for all the test cases.

Variable	Distribution	Range
T_e	Uniform	8000 K - 12000 K
p_e	Uniform	90 hPa - 210 hPa
p_d	Uniform	35 Pa - 75 Pa
T_w	Uniform	2350 K - 2750 K
E_1	Uniform	0 K - 1500 K
E_3	Uniform	0 K - 2500 K
E_4	Uniform	0 K - 15000 K
E_5	Uniform	10000 K - 25000 K
E_6	Uniform	20000 K - 30000 K
$\log(X_3)$	Uniform	-2.5 - 0
$\log(X_4)$	Uniform	-4 - 0
$\log(X_5)$	Uniform	-4 - 0
$\log(X_6)$	Uniform	7.5 - 10.5
$\log(B)$	Uniform	-7 - -4

Table 5.2: Distributions of the parameters from which the LHS training points have been sampled.

Training points have been sampled once again using LHS technique.
The scheme of the numerical simulations used for obtaining the solution of the training points is shown below.

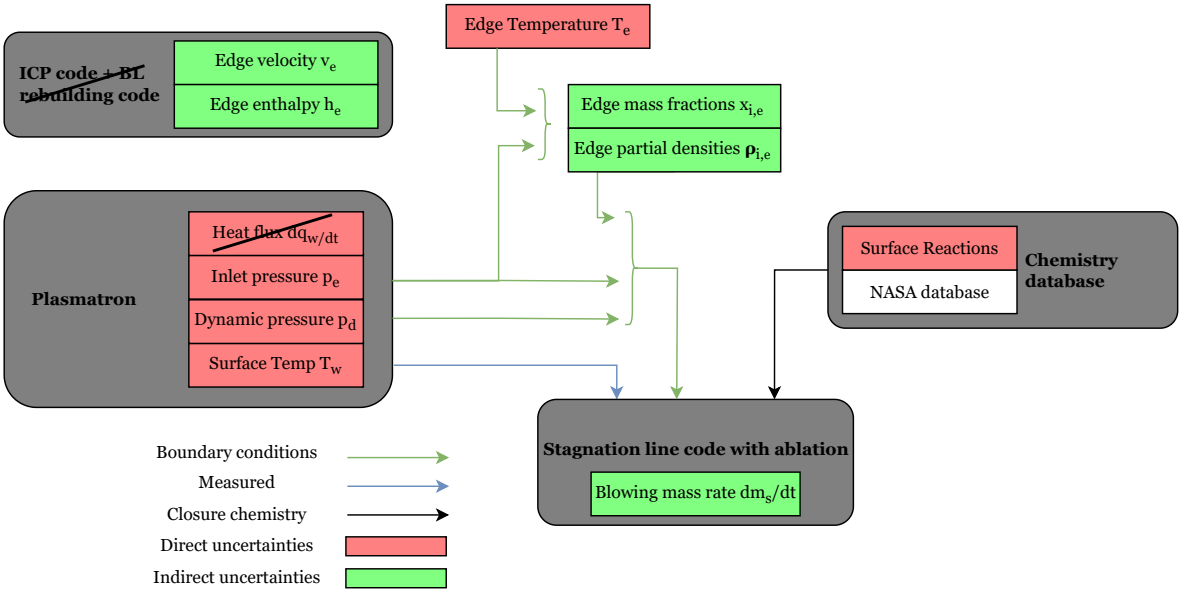

Figure 5.22: Scheme of the numerical simulations for the propagation of model and experimental uncertainties.

The Kriging model is trained once again using UQlab [23] and the neural network is trained similarly to what has been done for the 4-variable model. Once again, data are normalised according to the technique detailed in Section 5.1. The only major difference being the fact that three hidden layers have been used instead of two. The enlargement of the structure of the network is due to the increased number of variable of the new model. In the case of the four parameter models, presented in Section 5.1, it has been possible to obtain valid surrogate models using both the Kriging formulation and an artificial neural network scheme with the mean square error on an independent test set of 200 samples being less than 2% for a training set of around 800 samples.
In the case of the 14-parameter model needed to propagate model and experimental un-

certainties at the same time, the error on an independent set of test points (150) obtained using a neural network is significantly smaller with respect to the one obtained using a Kriging model considering the same number of samples. It reaches a value around the 2% mark with 6000 training samples, whereas the error obtained with the Kriging model trained on the same number of samples is still larger than 15%.
The "optimised" number of neurons per layer is 13, 14, 14.

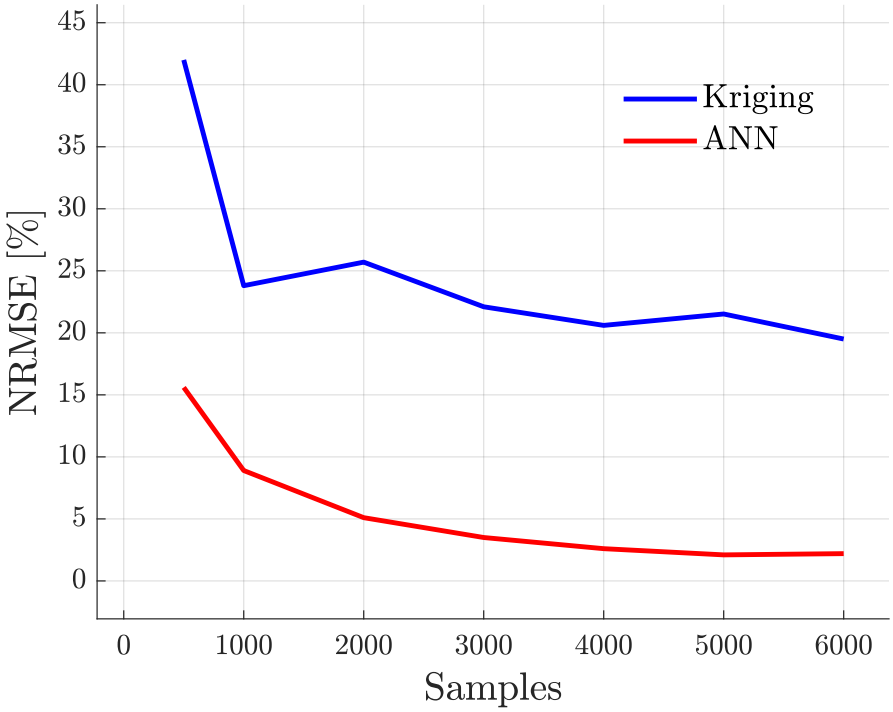

Figure 5.23: Convergence of the normalised root mean square error (NRMSE) between models predictions and full numerical solution for a test set of 150 samples. The full numerical solutions obtained with the "optimised" ANN model are compared with full numerical solutions obtained using Capriati ablation model.

.

It seems that the Kriging models find it more difficult to replicate the behaviour of the full numerical solver when an high-dimensional input space is considered.
Two *qqplots* of the ANN model are displayed in Figure 5.24 and Figure 5.25. For the G8_100_400 case, 800 LHS samples have been drawn from a population described as:

- T_e: uniform distribution ranging from 8000 K to 12000 K;
- p_e: normal distribution centered at 200 hPa with 1.5% standard deviation;

- p_d: normal distribution centered at the nominal value of the experiment (see Table 4.3) with 1% standard deviation;
- T_w: normal distribution centered at the nominal value of the experiment (see Table 4.3) with 0.5% standard deviation.
- Rates $[E_1, E_3, E_4, E_5, E_6, X_3, X_4, X_5, X_6, B]$ from the Capriati version of the model using the mean values of the distribution.

This sampling mimics the 4-parameter model studied in Section 5.1. Full numerical solutions are compared with predictions of the ANN model. Ideal line (bisector) and a 2% error range is displayed.
In the case of the G1_200_370 experimental test, 800 samples have been drawn as follows:

- T_e: uniform distribution ranging from 8000 K to 12000 K;
- p_e: normal distribution centered at 200 hPa with 1.5% standard deviation;
- p_d: normal distribution centered at nominal value of the experiment (see Table 4.3) with 1% standard deviation;
- T_w: normal distribution centered at nominal value of the experiment (see Table 4.3) with 0.5% standard deviation.
- Rates $[E_1, E_3, E_4, E_5, E_6, X_3, X_4, X_5, X_6, B]$ are drawn from a population whose joint probability distribution is the one obtained by Capriati Markov Chain Monte Carlo analysis (PDFs of the single variables are reported in Appendix A).

Both *qqplots* are good confirmations of the validity of the ANN surrogate models.

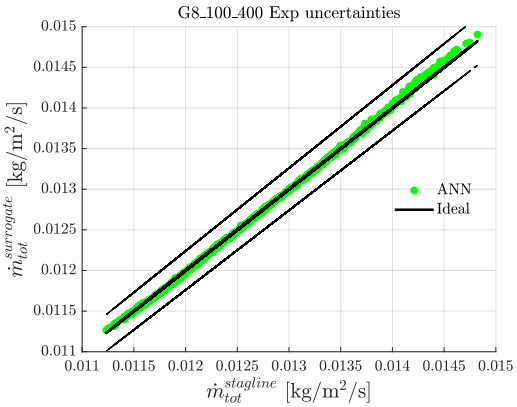

Figure 5.24: *Qqplot* for the G8_100_370 test case. Comparison between full numerical solutions obtained and the predictions of the ANN surrogate models for 800 samples drawn from a population describing the experimental uncertainties of the test case considered. Rates describing chemical GSI interactions are kept fixed.

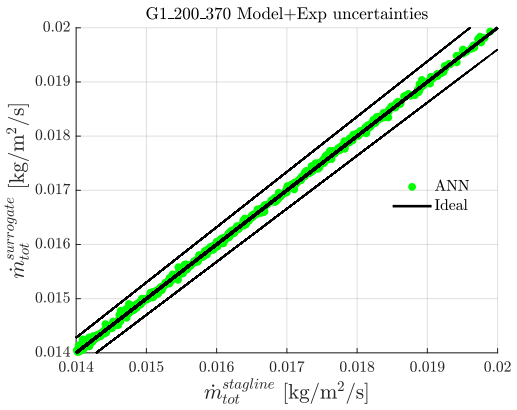

Figure 5.25: *Qqplot* for the G1_200_370 test case. Comparison between full numerical solutions obtained and the predictions of the ANN surrogate models for 800 samples drawn from a population describing both experimental uncertainties of the test case considered and probability distributions obtained by Capriati for the ablation rates.

Alongside *qqplots*, analyses on the PDFs of the G1_200_370 experimental test and G8_100_400 experimental test are reported in Figures 5.26-5.29. PDFs obtained with the full numerical solutions used for the *qqplots* are compared with realisations of the surrogate models for a larger number of samples drawn from the same distributions. Capriati's mean values of the rates are kept fixed for the PDFs in yellow, whereas rate samples are drawn from the MCMC distributions for the PDFs in blue.

The comparison between the realisations of the ANN surrogate models and the full numerical solutions proves once more the validity of the model; Kriging model realisations display error with respect to the full simulations. More in particular, it seems that the tails of the PDFs are the regions where one can notice the largest differences between realisations of the surrogate models and the full numerical solutions. Differences are in line with the estimated error on the training set.

The poor rate of convergence of the error on the test set of the Kriging model may be attributed to the fact that samples drawn as described above do not fully respect LHS sampling procedure, given that the 14- dimension input space is divided in two. Values of the model variables assigned to samples whose experimental variables do come from LHS sampling have been sampled according to no particular rules deriving from the MCMC

process performed by Capriati.

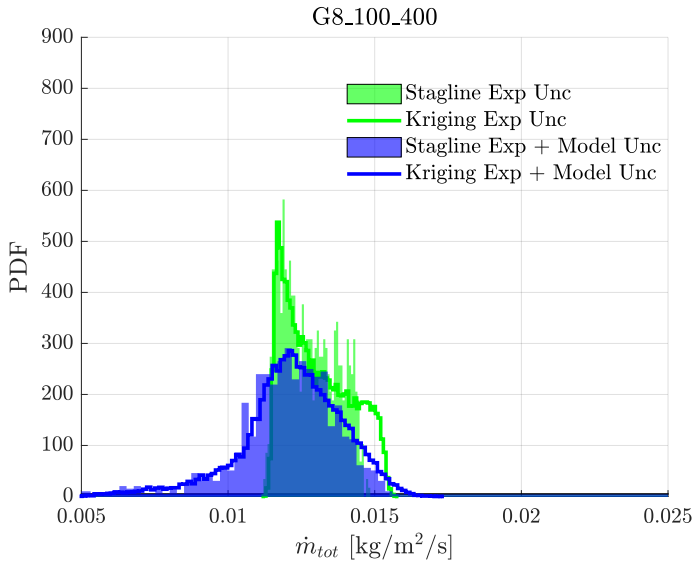

Figure 5.26: Test case G8_100_400. PDFs obtained from full numerical solutions of samples drawn from a population describing experimental uncertainties (yellow) and from one describing both numerical and experimental uncertainties (blue) are compared with converged PDFs obtained from solutions of samples drawn from the same distributions using Kriging surrogate model.

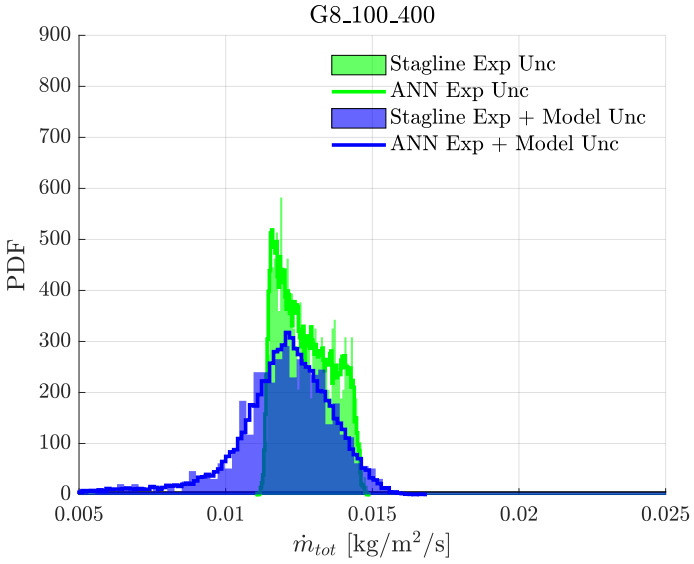

Figure 5.27: Test case G8_100_400. PDFs obtained from full numerical solutions of samples drawn from a population describing experimental uncertainties (yellow) and from one describing both numerical and experimental uncertainties (blue) are compared with converged PDFs obtained from solutions of samples drawn from the same distributions using ANN surrogate model.

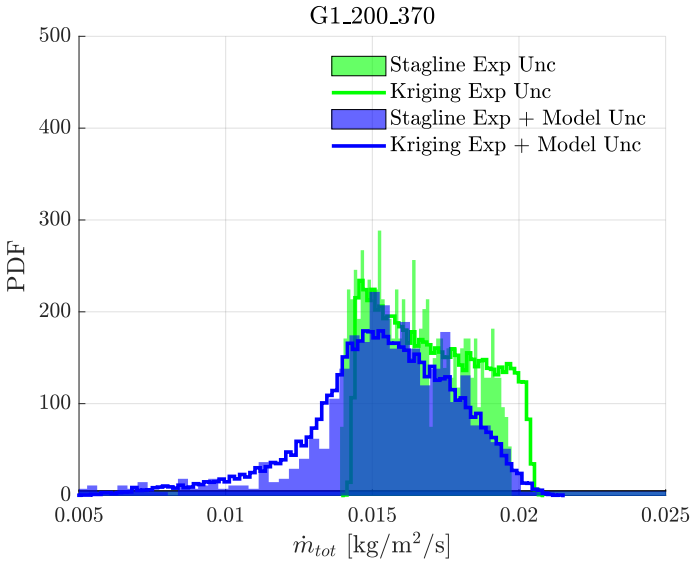

Figure 5.28: Test case G1_200_370. PDFs obtained from full numerical solutions of samples drawn from a population describing experimental uncertainties (yellow) and from one describing both numerical and experimental uncertainties (blue) are compared with converged PDFs obtained from solutions of samples drawn from the same distributions using ANN surrogate model.

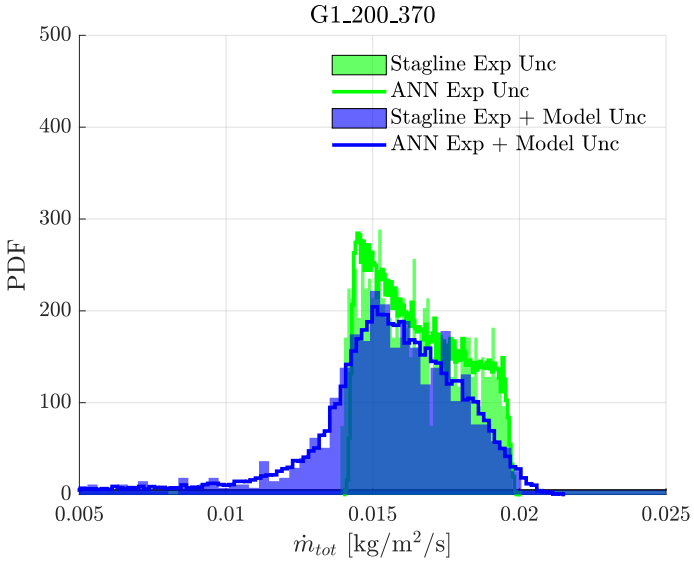

Figure 5.29: Test case G1_200_370. PDFs obtained from full numerical solutions of samples drawn from a population describing experimental uncertainties (yellow) and from one describing both numerical and experimental uncertainties (blue) are compared with converged PDFs obtained from solutions of samples drawn from the same distributions using ANN surrogate model.

The comparison of the PDFs and the *qqplots* have shown that the 14-parameter surrogate model can be used to propagate experimental uncertainties only and both model and experimental uncertainties with a sufficiently small error. It can be said that the 4-parameter model obtained in Section 5.1 is "contained" in the 14-parameter one, as it should be.
It is then interesting to understand how the interpercentile ranges widen when considering both numerical and model uncertainties rather than experimental uncertainties only.
This is done in Figure 5.30, that shows the propagation of the experimental uncertainties compared with the propagation of model and experimental uncertainties for all eight test cases using the ANN 14-parameter model. Solid line bars are associated to the uncertainties on the experimental results. As in previous Figures, bars represent the interpercentile range of the associated distribution.

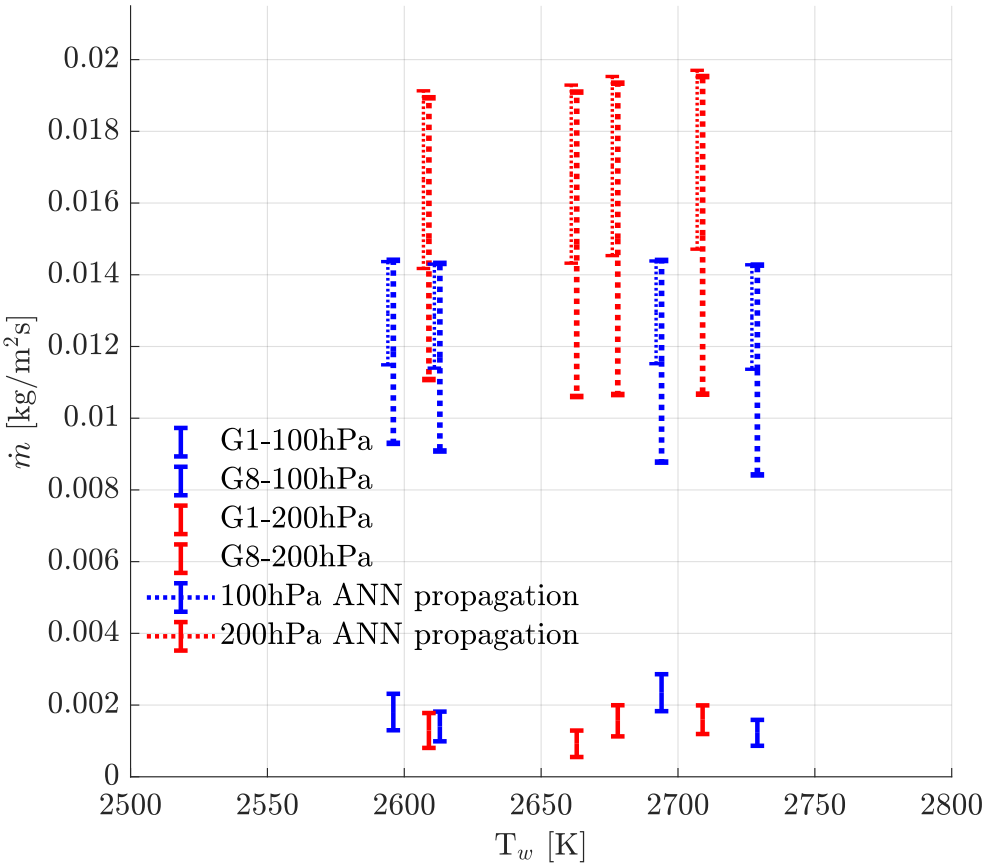

Figure 5.30: Comparison between the propagation of uncertainties using ANN 14-parameter model and experimental results for higher pressure campaign. Thin dashed lines represent the propagation of experimental uncertainties. Thick dashed lines are the propagation of model and experimental uncertainties combined. Solid line represents uncertainties on experimental results. Interpercentile ranges are displayed for all the distributions.

As expected, interpecentile ranges for the combined propagation of experimental and model uncertainties are wider than the ones for the propagation of experimental results only. It would have been desirable that the interpercentile ranges at least partially intercept the uncertainties on the experimental blowing mass rate; nonetheless, it is not the case.

Finally, an analysis similar to the one just presented has been performed acting as a sort of validation of the techniques used.

Instead of performing a *pseudo*-LHS sampling with the values assigned to the rate coefficients coming from the MCMC chain of Capriati and the experimental variables actually

being drawn with a LHS sampling technique, a proper LHS sampling technique have been used to draw samples from the population used for the training of the ANN 14-parameter model detailed in Table 5.2 .

Ranges have been selected so as to properly draw samples from the distribution obtained by Capriati. Nonetheless, they include the values of the rate coefficient proposed by Prata for almost all the variables outside of two (X_3 and E_1).

It is then expected, if the procedures used are correct, that the interpercentile ranges obtained from the propagation stretch the ones obtained sampling from the distribution obtained by Capriati possibly so far as to partially include the experimental uncertainties. This is shown in Figure 5.31, where medium dashed lines represent the propagation of experimental uncertainties; thick dashed lines are the propagation of model and experimental uncertainties combined; thin dashed lines combines propagation of experimental uncertainties and LHS sampling of the training ranges of the ANN model for the 10 variables of the ablation model and solid line represents uncertainties on experimental results.

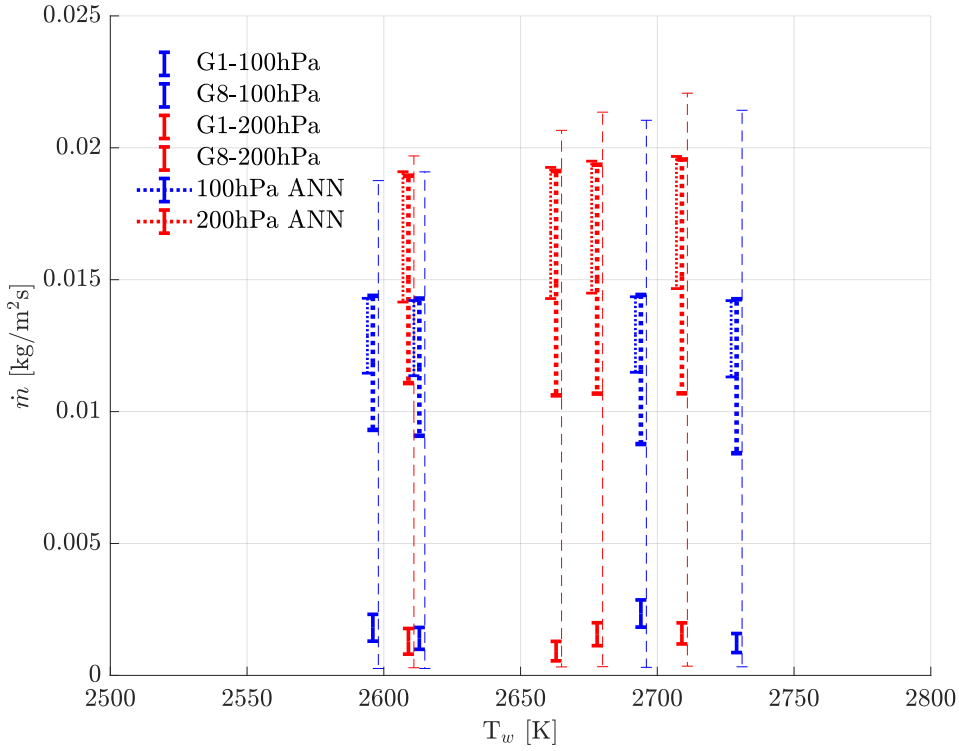

Figure 5.31: Further comparison between the propagation of uncertainties using ANN 14-parameters model and experimental results for higher pressure campaign. Medium dashed lines represent the propagation of experimental. Thick dashed lines are the propagation of model and experimental uncertainties combined. Thin dashed lines combines propagation of experimental uncertainties and LHS sampling of the training ranges of the ANN model for the 10 variables of the ablation model. Solid line represents uncertainties on experimental results. Interpercentile ranges are displayed for all the distributions.

A brief sensitivity analysis on the ANN 14-parameter model has been performed.
Sobol indices have been computed using UQlab with the Monte Carlo technique. It is noticeable that for this model higher order indices play a relevant role, meaning that combined effects between the input variables do affect the output of the model. Moreover, only 6 of the 14 input variables have a relevant Sobol index. These are all model variable. A similar Sobol analysis have been obtained by Capriati [6] when analysing the same 14-parameter model in a lower range of pressures.

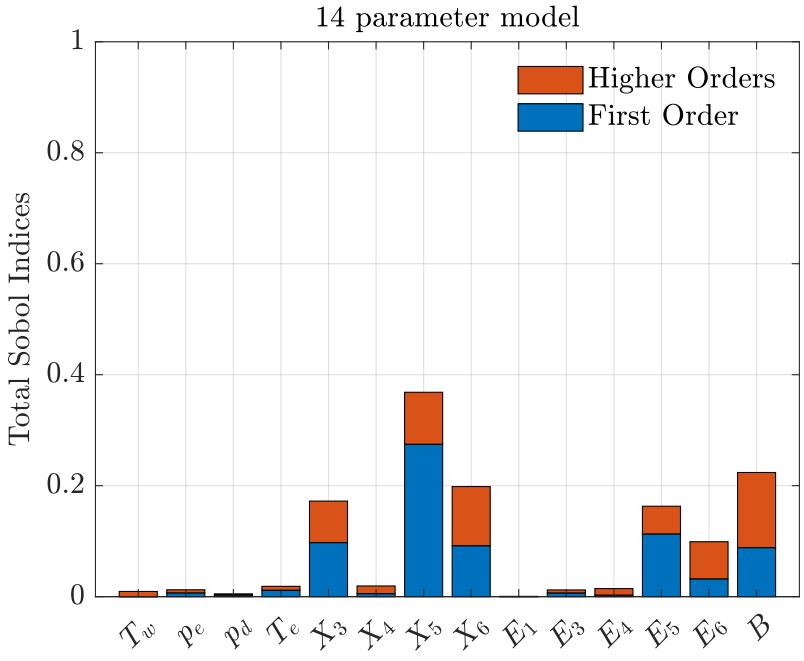

Figure 5.32: Total Sobol Indices of ANN surrogate model.

5.4. Summary

The last chapter of this work has been dedicated to the quantification of the uncertainties in the simulations of the second experimental campaign using Prata's and Capriati's versions nitrogen-carbon ablation model.

The propagation of experimental uncertainties (4-parameter models) and experimental and model uncertainties combined (14-parameter models) has shown that Prata's version is more accurate than Capriati's one in describing gas-surface interactions at higher pressures (100 and 200 hPa), contrary to the what happens at lower pressures (15 hPa).

A detailed sensitivity analysis of the 4-parameter surrogate models has shown the difference between the two ablation models in terms of favoured chemical pathways and variation of the blowing mass rate with respect to the input variables.

It has been seen that the performance of neural network surrogate models and Kriging models are comparable for the 4-parameter models; on the contrary, it has been shown that neural network outperforms the Kriging model when the 14-parameter model is considered.

A validation of the previous analysis has been performed propagating a wide range of values encompassing all the values for the rate coefficients of the surface reaction proposed by Capriati and almost all the values for the same parameters proposed by Prata.

Finally, a brief analysis on the Sobol indices of the ANN 14-parameter model is presented.

6 | Conclusions and future developments

The primary objective of this work was the validation of a Nitrogen-Carbon ablation model proposed by Capriati; the model is an updated version of a subset of the ACA model proposed by Prata. The two models differ for the values of the rate coefficients used to describe the chemical reactions occurring at the surface of carbon-based materials. The coefficients of Prata were obtained deterministically, whereas Capriati derived them employing a Bayesian technique, allowing to infer their uncertainties. The accuracy of the model was assessed by numerically simulating two experimental campaign performed in the VKI Plasmatron, a unique ICP wind tunnel.

Such assessment has been carried out forward propagating the uncertainties on the input of the models with the scope of comparing the uncertainties on the output of the simulations with their experimental counterparts. The uncertainties on the rate coefficients proposed by Capriati have also been propagated.

These analyses have shown that the model proposed by Capriati compared to the original model, improves the prediction of the experiments of the first testing campaign, performed at 15hPa of chamber pressure.

On the other hand, the model of Prata does a better job at predicting the mass blow rate experimentally observed in the second campaign; the simulations of this campaign with the model proposed by Capriati predict higher values.

The propagation of the uncertainties has been performed employing both a Kriging model and a Neural Network. They show similar results for the propagation of the experimental uncertainties (4-parameter models). Similar errors on independent validation points for the same number of training points was obserbed, with the Kriging error being lower. On the other hand, it has been shown that a neural network model significantly outperforms the Kriging model when the dimensionality of the input is increased to 14. In fact, the error associated to the neural network was times lower than the one relative to the Kriging model for the same number of training points

The analysis highlights the necessity to further improve the model predictions at pres-

sures higher than 15 hPa. Such a refinement could be achieved constructing a new Markov Chain Monte Carlo method including observations relative to the experimental campaign at higher pressures.
The second campaign has shown smaller influence of the wall temperature on the mass production rate than the first campaign.
Furthermore, the second testing campaign, characterised by significantly higher pressures, shows lower mass production rates lower than the ones observed in the first testing campaign. This behaviour is not in accordance with the rather strong pressure dependence predicted by the model of Capriati.
Based on these two evidences, one may suggest to perform another set of experiments with similar conditions to the ones of the second campaign, so as to verify whether the proportionality between the wall temperature and the mass production rate is physical; it would also allow to get an insight on the proportionality, or on the lack of it, between pressure and the mass production rate.
In case this hypothetical new testing campaign shows results that are comparable with the one already performed, one should then use a set of observations including all the results collected in the Plasmatron for assessing model predictions.

Bibliography

[1] D. V. Abeele and G. Degrez. Efficient computational model for inductive plasma flows. *AIAA Journal*, pages 234–242, 2000.

[2] J. Anderson. *Hypersonic and High Temperature Gas Dynamics*. McGraw Hill, New York, 1989.

[3] P. F. Barbante, G. Degrez, and G. S. R. Sarma. Computation of nonequilibrium high-temperature axisymmetric boundary-layer flows. *Journal of Thermophysics and Heat Transfer*, pages 490–497, 2002.

[4] A. Bottin, M. Carbonaro, V. Haegen, and S. Paris. Predicted & measured capability of the vki 1. 2 mw plasmatron regarding re-entry simulation. *Aerothermodynamics for space vehicles, Proceedings of the 3rd European Symposium on Aerothermodynamics for space vehicles held at ESTEC, Noordwijk*, page 553, 1999.

[5] B. Bottin, D. V. Abeele, M. Carbonaro, G. Degrez, and G. S. R. Sarma. Thermodynamic and transport properties for inductive plasma modeling. *Journal of Thermophysics and Heat Transfer*, pages 169–187, 1999.

[6] M. Capriati. *Multi-fidelity Bayesian inference of hypersonic flow free-stream conditions and heterogeneous chemistry model parameters*. PhD thesis, École Polytechnique et au Département d'aéronautique et d'aérospatiale de l'Institut von Karman de dynamique des fluides, 2024.

[7] M. Capriati, A. del Val, T. Schwartzentruber, T. Minton, P. Congedo, and T. E. Magin. Bayesian calibration of a finite-rate nitridation model from molecular beam and plasma wind tunnel experiments. In *Aerospace Europe Conference*. 10th EUCASS-9th CEAS, 2023.

[8] S. Chapman and T. Cowling. *The Mathematical Theory of Non-uniform Gases: An Account of the Kinetic Theory of Viscosity, Thermal Conduction and Diffusion in Gases*. Cambridge University Press, 1970.

[9] J. Cleland and F. Iannetti. Thermal protection system of the space shuttle. *NASA Contractor Report*, 1989.

[10] R. Crowder and J. Moote. Apollo entry aerodynamics. *North American Rockwell Corporation*, 1969.

[11] G. Degrez, D. V. Abeele, P. Barbante, and B. Bottin. Numerical simulation of inductively coupled plasma flows and hypersonic (re-) entry flows. In *ECCOMAS 2000*. European Congress on Computational Methods in Applied Sciences and Engineering, 2000.

[12] I. Goodfellow, Y. Bengio, and A. Courville. *Deep Learning*. MIT Press, 2016. `http://www.deeplearningbook.org`.

[13] B. Helber, O. Chazot, A. Hubin, and T. E. Magin. Emission spectroscopic boundary layer investigation during ablative material testing in plasmatron. *JoVE Journal*, 2016.

[14] B. Helber, A. Turchi, and T. E. Magin. Determination of active nitridation reaction efficiency of graphite in inductively coupled plasma flows. *Carbon*, pages 582–594, 2017.

[15] F. Herning and L. Zipperer. Calculation of the viscosity of technical gas mixtures from the viscosity of the individual gases. *Gas and Waterfach*, pages 49–54, 1936.

[16] S. Kawai and K. Shimoyama. Kriging-model-based uncertainty quantification in computational fluid dynamics. *AIAA Journal*, 2014.

[17] A. Klomfass and S. Muller. Calculation of stagnation streamline quantities in hypersonic blunt body flows. *Shock Waves*, 10 1996.

[18] A. Kolesnikov. Conditions of simulation of stagnation point heat transfer from a high-enthalpy flow. *Fluid Dynamics*, pages 131–137, 1993.

[19] D. Lee and W. Goodrich. The aerothermodynamic environment of the apollo command module during superorbital entry. *NASA Technical Note*, 1972.

[20] B. Lockwood, M. Rumpfkeil, W. Yamazaki, and D. Mavriplis. Uncertainty quantification in viscous hypersonic flows using gradient information and surrogate modeling. *AIAA Journal*, 2012.

[21] R. Lorenz, E. Turtle, J. Barnes, M. Trainer, D. Adams, K. Hibbard, C. Sheldon, K. Zacny, P. Peplowski, D. Lawrence, M. A. Ravine, T. McGee, K. Sotzen, S. MacKenzie, J. Langelaan, S. Schmitz, L. Wolfarth, and P. Bedini. Dragonfly: A

rotorcraft lander concept for scientific exploration at titan. Technical report, APL Research and Development, 10 2018.

[22] T. E. Magin. Plasmut - nonequilibrium gas-surface interactions at high temperature, vki plasmatron and mutation++ library. Technical report, von Karman Institute for fluid dynamics, 3 2023.

[23] S. Marelli and B. Sudret. Uqlab: A framework for uncertainty quantification in matlab. *Vulnerability, Uncertainty, and Risk: Quantification, Mitigation, and Management*, pages 2554–2563, 2014. doi: 10.1061/9780784413609.257.

[24] D. W. Marquardt. An algorithm for least-squares estimation of nonlinear parameters. *Journal of the Society for Industrial and Applied Mathematics.*, 11:431–441, 1963.

[25] S. Matsuyama, N. Ohnishi, S. Akihiro, and K. Sawada. Numerical simulation of galileo probe entry flowfield with radiation and ablation. *Journal of Thermophysics and Heat Transfer*, 2005.

[26] B. McBride, M. Zehe, and G. S. Nasa glenn coefficients for calculating thermodynamic properties of individual species. Technical report, NASA, 9 2002.

[27] M. McKay, R. Beckman, and W. Conover. A comparison of three methods for selecting values of input variables in the analysis of output from a computer code. *Technometrics*, pages 239–245, 1979.

[28] N. Metropolis and S. Ulam. The monte carlo method. *Journal of the American Statistical Association*, pages 335–341, 1949.

[29] A. Munafò. *Multi-Scale Models and Computational Methods for Aerothermodynamics*. PhD thesis, École Centrale Paris, 2014.

[30] C. Park. *Nonequilibrium Hypersonic Aerothermodynamics*. Springer Berlin Heidelberg, 1990.

[31] K. S. Prata, T. Schwartzentrubera, and T. Mintonb. Air-carbon ablation model for hypersonic flight from molecular beam data. *AIAA Journal*, 2022.

[32] A. Rasamoelina, F. Adjailia, and P. Sinčák. A review of activation function for artificial neural network. *2020 IEEE 18th World Symposium on Applied Machine Intelligence and Informatics (SAMI)*, pages 281–286, 2020.

[33] B. Richards and K. Enkenhus. Hypersonic testing in the vki longshot free- piston tunnel. *AIAA journal*, 4, 1970.

[34] M. Richiardi, R. Leombruni, N. Saam, and M. Sonessa. A primer on sensitivity analysis of agent-based models. *Journal of Artificial Societies and Social Simulation*, 2006.

[35] P. Rini, D. V. Abeele, and G. Degrez. Closed form for the equations of chemically reacting flows under local thermodynamic equilibrium. *Phys. Rev.*, 2005.

[36] T. Santner, B. Williams, and W. Notz. *The design and analysis of computer experiments.* Springer, 2003.

[37] I. Sobol. Global sensitivity indices for nonlinear mathematical models and their monte carlo estimates. *Mathematics and Computers in Simulation*, 35:271–280, 2001.

[38] I. Sobol. Spatial modelling with the matérn correlation function. *Georg Lindgren, Hans Rue, Johan Lindström*, 38:36–38, 2011.

[39] J. Stefan and J. Maxwell. Zur theorie der verdampfung. *Annalen der Physik und Chemie*, pages 100–103, 1874.

[40] J. Steinfeld, J. Francisco, and W. Hase. *Chemical Kinetics and Dynamics*. Prentice Hall, 1998. ISBN 978-0137371230.

[41] W. Vincenti and C. Kruge. *Introduction to physical gas dynamics*. Krieger Publishing Company, 1965.

[42] M. Wright, K. Edquist, C. Tang, B. Hollis, P. Krasa, and C. Campbell. A review of aerothermal modeling for mars entry missions. *Proceedings of the 48th AIAA Aerospace Sciences Meeting Including the New Horizons Forum and Aerospace Exposi- tion*, 2010.

A | Appendix A

Below are reported the expression of the transport matrices:

CHECK IF IT IS REALLY NECESSARY TO PUT THEM

$$G_{ij}^{V} = -\frac{X_i X_j}{D_{ij}}(1+\phi_{ij}), \quad i \neq j \tag{A.1}$$

$$G_{ii}^{V} = \sum_{j\neq i, j\in\mathcal{H}} \frac{X_i X_j}{D_{ij}}(1+\phi_{ij}) + \left(\frac{T_e}{T}\right)\frac{X_i X_e}{D_{ie}}(1+\phi_{ie}), \tag{A.2}$$

$$G_{ij}^{\mu} = G_{ji}^{\mu} = \frac{X_i X_j}{nD_{ij}}\frac{1}{m_i+m_j}\left(\frac{6}{5}\frac{Q_{i,j}^{(2,2)}}{Q_{i,j}^{(1,1)}} - 2\right), \quad i \neq j \tag{A.3}$$

$$G_{ij}^{\mu} = G_{ji}^{\mu} = \sum_{j\neq i, j\in\mathcal{H}} \frac{X_i X_j}{nD_{ij}}\frac{1}{m_i+m_j}\left(\frac{6}{5}\frac{m_j}{m_i}\frac{Q_{i,j}^{(2,2)}}{Q_{i,j}^{(1,1)}} + 2\right) + \frac{X_i^2}{\mu_i}, \tag{A.4}$$

$$G_{ij}^{\lambda^T} = G_{ji}^{\lambda^T} = \frac{1}{25k_B}\frac{X_i X_j}{nD_{ij}}\frac{m_i m_j}{(m_i+m_j)^2}\left(16\frac{Q_{i,j}^{(2,2)}}{Q_{i,j}^{(1,1)}} + 12\frac{5Q_{i,j}^{(1,2)} - 4Q_{i,j}^{(1,3)}}{Q_{i,j}^{(1,1)}} - 55\right), \quad i \neq j \tag{A.5}$$

$$G_{ii}^{\lambda^T} = G_{ji}^{\lambda^T} = \frac{1}{25k_B}\sum_{j\neq i, j\in\mathcal{H}}\left(30\frac{m_i^2}{m_j^2} + 25\frac{m_j}{m_i} - 12\frac{m_j}{m_i} + 16\frac{Q_{i,j}^{(2,2)}}{Q_{i,j}^{(1,1)}} - 12\frac{5Q_{i,j}^{(1,2)} - 4Q_{i,j}^{(1,3)}}{Q_{i,j}^{(1,1)}}\right)\cdot \cdot\frac{X_i X_j}{nD_{ij}}\frac{m_i m_j}{(m_i+m_j)^2} + \frac{4}{15k_B}\frac{X_i^2 m_i}{\mu_i} \tag{A.6}$$

(A.7)

The following figures show the recorded wall temperature over time for the second testing campaign. Above the raw experimental data, the exponential approximation is plotted as a red dashed line.

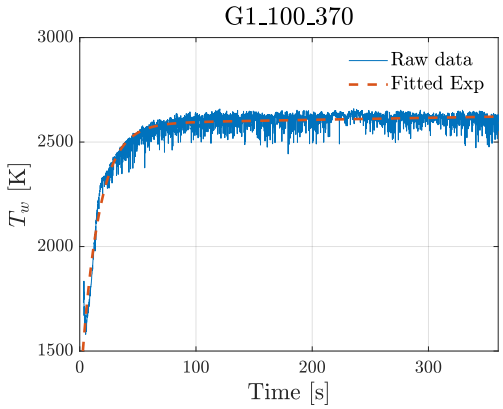
G1_100_370
Raw data
Fitted Exp
T_w [K]
Time [s]
3000
2500
2000
1500
0
100
200
300

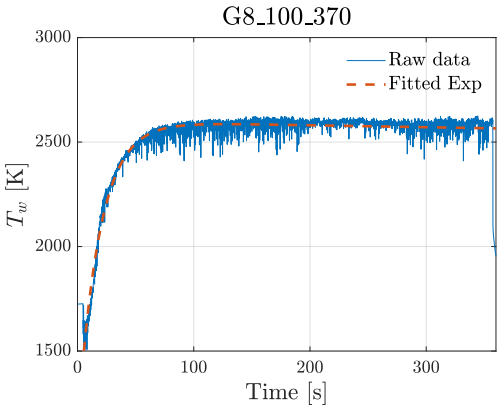
G8_100_370
Raw data
Fitted Exp
T_w [K]
Time [s]
3000
2500
2000
1500
0
100
200
300

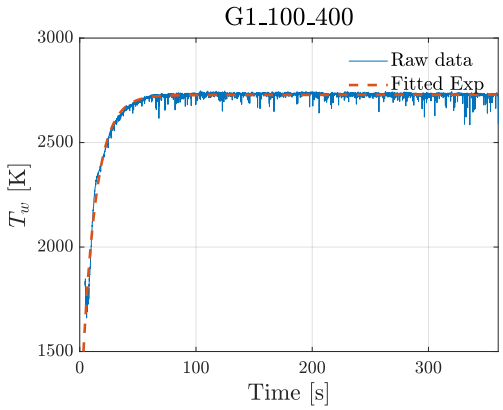
G1_100_400
Raw data
Fitted Exp
T_w [K]
Time [s]
3000
2500
2000
1500
0
100
200
300

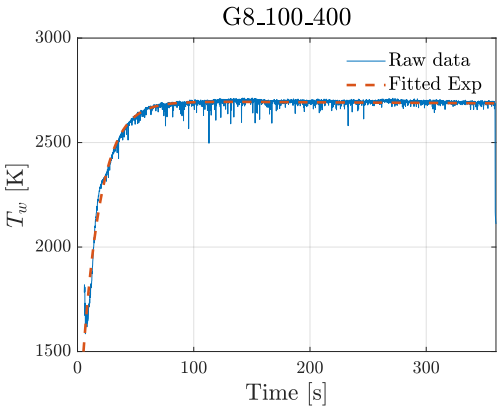
G8_100_400
Raw data
Fitted Exp
T_w [K]
Time [s]
3000
2500
2000
1500
0
100
200
300

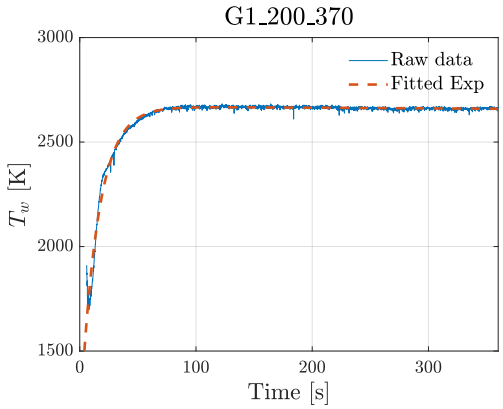
G1_200_370
Raw data
Fitted Exp
T_w [K]
Time [s]
3000
2500
2000
1500
0
100
200
300

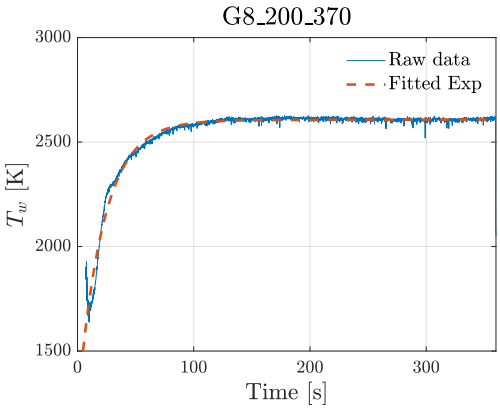
G8_200_370
Raw data
Fitted Exp
T_w [K]
Time [s]
3000
2500
2000
1500
0
100
200
300

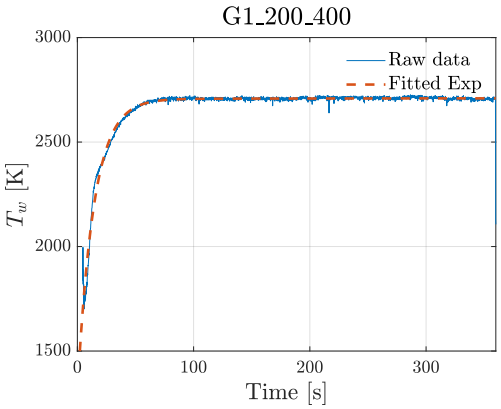

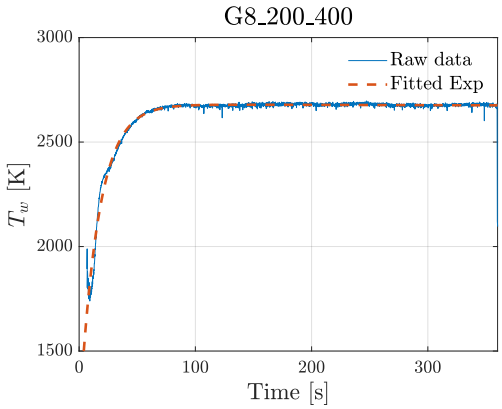

Below are reported the probability distribution functions (PDF) distributions of the rates describing the chemical interactions between Nitrogen flow and Carbon surfaces obtained by Capriati as a result of a Markov Chain Monte Carlo process [6]. The punctual value for each of the rates proposed by Capriati is the mean value of the distribution, highlighted using a dashed blue line.

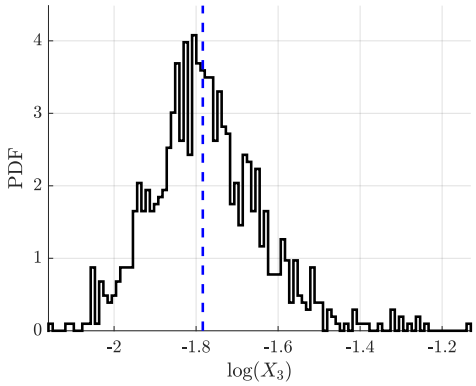

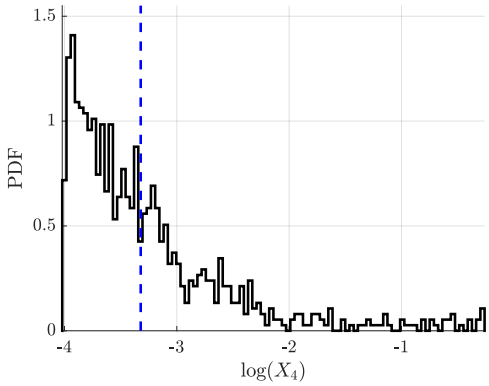

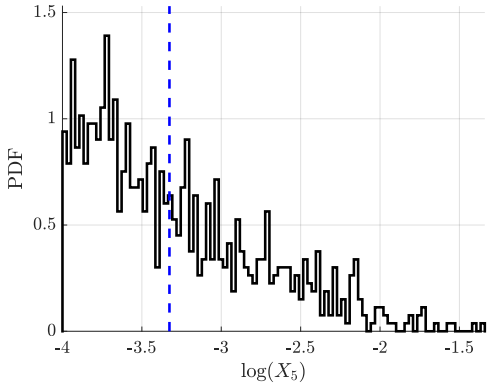

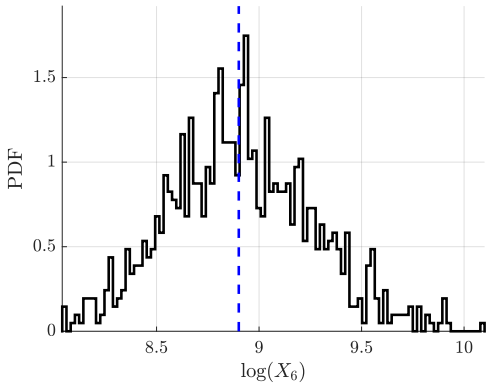

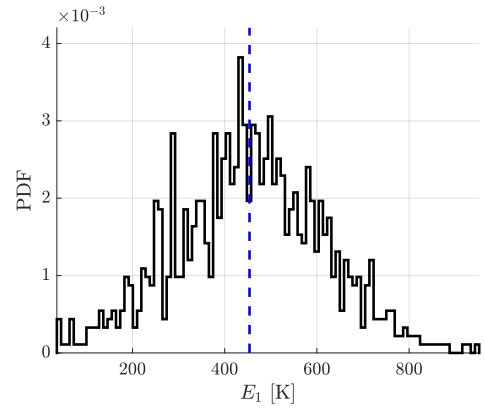
×10^−3
PDF
E1 [K]

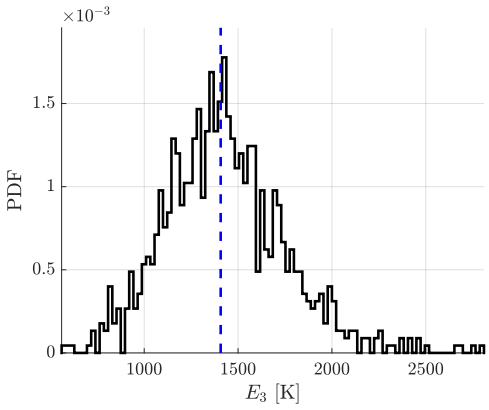
×10^−3
PDF
E3 [K]

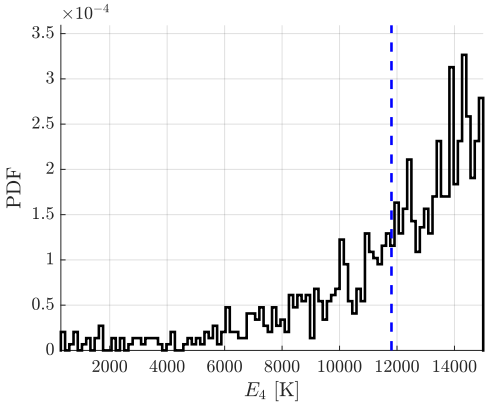
×10^−4
PDF
E4 [K]

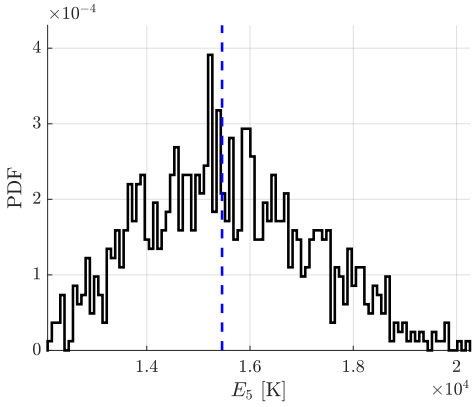
×10^−4
PDF
E5 [K]
×10^4

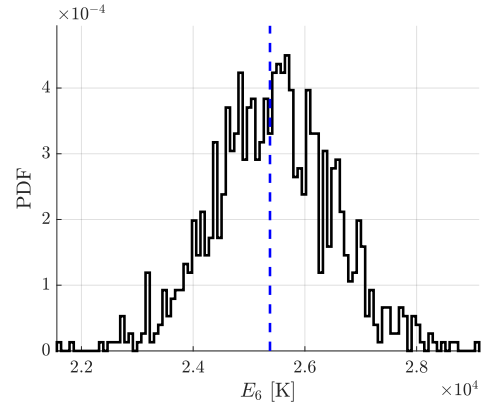
×10^−4
PDF
E6 [K]
×10^4

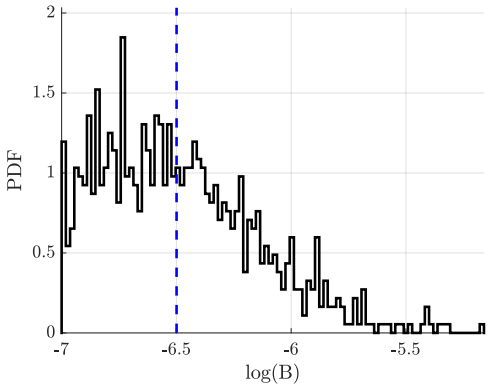
PDF
log(B)

List of Figures

List of Tables

Acknowledgements

A word of thanks to all the professors who helped me in this work, in particular to the supervisors of this thesis, professor Vigevano, professor Arnst, and professor Magin. I would like to express my sincere gratitude to Michele Capriati and Federico Bariselli for guiding me during the internship in the von Karman Institute.
Due thanks to the three institutions that made this work possible.
A special thank you to Politecnico di Milano for shaping my mind during four intense years, and for making my experience abroad financially possible co-operating with the Erasmus+ program.
Thank you to Université de Liège for hosting me, for giving me the possibility of expanding my knowledge, and for opening doors to the world around me.
A final thank you to von Karman Institute for giving me the opportunity to deal with cutting edge research topics.
I am glad I had the chance of meeting many friends along the way. I here want to thank them all.
A special thank you to my family, for always being at my side and ready to support me.